A&A 629, A131 (2019)
https://doi.org/10.1051/0004-6361/201936250

Astronomy & Astrophysics

New constraints on the physical conditions in H_2-bearing GRB-host damped Lyman-α absorbers[⋆,⋆⋆]

K. E. Heintz[1], J. Bolmer[2], C. Ledoux[3], P. Noterdaeme[4], J.-K. Krogager[4], J. P. U. Fynbo[5,6], P. Jakobsson[1], S. Covino[7], V. D'Elia[8,9], M. De Pasquale[10], D. H. Hartmann[11], L. Izzo[12], J. Japelj[13], D. A. Kann[12], L. Kaper[13], P. Petitjean[4], A. Rossi[14], R. Salvaterra[15], P. Schady[2,16], J. Selsing[5,6], R. Starling[17], N. R. Tanvir[17], C. C. Thöne[12], A. de Ugarte Postigo[12], S. D. Vergani[18,4], D. Watson[5,6], K. Wiersema[17,19], and T. Zafar[20]

[1] Centre for Astrophysics and Cosmology, Science Institute, University of Iceland, Dunhagi 5, 107 Reykjavík, Iceland
e-mail: keh14@hi.is
[2] Max-Planck-Institut für Extraterrestrische Physik, Giessenbachstraße, 85748 Garching, Germany
[3] European Southern Observatory, Alonso de Córdova 3107, Vitacura, Casilla 19001 Santiago 19, Chile
[4] Institut d'Astrophysique de Paris, CNRS-SU, UMR7095, 98bis bd Arago, 75014 Paris, France
[5] Cosmic DAWN Center NBI/DTU-Space, Denmark
[6] Niels Bohr Institute, University of Copenhagen, Lyngbyvej 2, 2100 Copenhagen Ø, Denmark
[7] INAF – Osservatorio Astronomico di Brera, Via E. Bianchi 46, 23807 Merate, LC, Italy
[8] Space Science Data Center, SSDC, ASI, Via del Politecnico snc, 00133 Roma, Italy
[9] INAF – Osservatorio Astronomico di Roma, Via Frascati 33, 00040 Monteporzio Catone, Italy
[10] Department of Astronomy and Space Sciences, Istanbul University, Beyazit, 34119 Istanbul, Turkey
[11] Department of Physics and Astronomy, Clemson University, Clemson, SC 29634-0978, USA
[12] Instituto de Astrofísica de Andalucía (IAA-CSIC), Glorieta de la Astronomía s/n, 18008 Granada, Spain
[13] Anton Pannekoek Institute for Astronomy, University of Amsterdam, Science Park 904, 1098 XH Amsterdam, The Netherlands
[14] INAF – Osservatorio di Astrofisica e Scienza dello Spazio, Via Piero Gobetti 93/3, 40129 Bologna, Italy
[15] INAF – IASF/Milano, Via Corti 12, 20133 Milano, Italy
[16] Department of Physics, University of Bath, Claverton Down, Bath BA2 7AY, UK
[17] Department of Physics and Astronomy, University of Leicester, University Road, Leicester LE1 7RH, UK
[18] GEPI, Observatoire de Paris, PSL University, CNRS, Place Jules Janssen, 92190 Meudon, France
[19] Department of Physics, University of Warwick, Coventry CV4 7AL, UK
[20] Australian Astronomical Optics, Macquarie University, 105 Delhi Road, North Ryde, NSW 2113, Australia

Received 5 July 2019 / Accepted 6 August 2019

ABSTRACT

We report the detections of molecular hydrogen (H_2), vibrationally-excited H_2 (H_2^*), and neutral atomic carbon (C I), an efficient tracer of molecular gas, in two new afterglow spectra of GRBs 181020A ($z = 2.938$) and 190114A ($z = 3.376$), observed with X-shooter at the Very Large Telescope (VLT). Both host-galaxy absorption systems are characterized by strong damped Lyman-α absorbers (DLAs) and substantial amounts of molecular hydrogen with $\log N(\mathrm{H\,I}, \mathrm{H_2}) = 22.20 \pm 0.05$, 20.40 ± 0.04 (GRB 181020A) and $\log N(\mathrm{H\,I}, \mathrm{H_2}) = 22.15 \pm 0.05$, 19.44 ± 0.04 (GRB 190114A). The DLA metallicites, depletion levels, and dust extinctions are within the typical regimes probed by GRBs with $[\mathrm{Zn/H}] = -1.57 \pm 0.06$, $[\mathrm{Zn/Fe}] = 0.67 \pm 0.03$, and $A_V = 0.27 \pm 0.02$ mag (GRB 181020A) and $[\mathrm{Zn/H}] = -1.23 \pm 0.07$, $[\mathrm{Zn/Fe}] = 1.06 \pm 0.08$, and $A_V = 0.36 \pm 0.02$ mag (GRB 190114A). In addition, we examine the molecular gas content of all known H_2-bearing GRB-DLAs and explore the physical conditions and characteristics required to simultaneously probe C I and H_2^*. We confirm that H_2 is detected in all C I- and H_2^*-bearing GRB absorption systems, but that these rarer features are not necessarily detected in all GRB H_2 absorbers. We find that a large molecular fraction of $f_{H_2} \gtrsim 10^{-3}$ is required for C I to be detected. The defining characteristic for H_2^* to be present is less clear, though a large H_2 column density is an essential factor. We also find that the observed line profiles of the molecular-gas tracers are kinematically "cold", with small velocity offsets of $\delta v < 20\,\mathrm{km\,s^{-1}}$ from the bulk of the neutral absorbing gas. We then derive the H_2 excitation temperatures of the molecular gas and find that they are relatively low with $T_{ex} \approx 100$–300 K, however, there could be evidence of warmer components populating the high-J H_2 levels in GRBs 181020A and 190114A. Finally, we demonstrate that even though the X-shooter GRB afterglow campaign has been successful in recovering several H_2-bearing GRB-host absorbers, this sample is still hampered by a significant dust bias excluding the most dust-obscured H_2 absorbers from identification. C I and H_2^* could open a potential route to identify molecular gas even in low-metallicity or highly dust-obscured bursts, though they are only efficient tracers for the most H_2-rich GRB-host absorption systems.

Key words. galaxies: ISM – galaxies: high-redshift – ISM: molecules – dust, extinction – gamma-ray burst: general – gamma-ray burst: individual: 181020A and 190114A

⋆ Reduced spectra are also available at the CDS via anonymous ftp to cdsarc.u-strasbg.fr (130.79.128.5) or via http://cdsarc.u-strasbg.fr/viz-bin/cat/J/A+A/629/A131

⋆⋆ Based on observations collected at the European Southern Observatory, Paranal, Chile, under the Stargate consortium with Program ID: 0102.D-0662.

1. Introduction

Long-duration gamma-ray bursts (GRBs) are linked to the deaths of massive stars (see e.g., Woosley & Bloom 2006). These cosmological beacons originate at redshifts as high as $z \gtrsim 8$ (Salvaterra et al. 2009; Tanvir et al. 2009), and appear to be promising tracers of star formation, especially at high ($z \gtrsim 3$) redshifts (e.g., Greiner et al. 2015; Perley et al. 2016; Palmerio et al. 2019). GRBs are typically followed by a short-lived, multiwavelength afterglow emission (e.g., Mészáros 2006), which, when bright enough, can serve as a powerful probe of the conditions in the star-forming regions and the interstellar medium (ISM) in their host galaxies (Jakobsson et al. 2004; Fynbo et al. 2006; Prochaska et al. 2007). The absorption in GRB host galaxy lines of sight is typically found to be highly neutral-hydrogen-rich (Vreeswijk et al. 2004; Watson et al. 2006; Fynbo et al. 2009) and most of them are classified as damped Lyman-α absorbers (DLAs; Wolfe et al. 1986). These systems are similar to those previously observed in the spectra of bright quasars, which are produced by intervening galaxies in the line of sight. The DLAs provide the most effective and detailed probe of neutral gas at high redshifts (see e.g., Wolfe et al. 2005, for a review). GRB host-galaxy absorbers are among the strongest DLAs, probing the central-most regions of their hosts, compared to typical quasar DLAs that are more likely to probe the outskirts of the intervening galaxies (Fynbo et al. 2009). This makes GRB-DLAs the ideal probes of the ISM in high-redshift star-forming galaxies (reaching $z \sim 8$, e.g., Salvaterra 2015; Bolmer et al. 2018; Tanvir et al. 2018).

Given their direct link to star formation and the very high column densities of neutral gas typically detected in GRB afterglow spectra (e.g., Jakobsson et al. 2006), it was anticipated that most GRB absorbers would show the presence of molecular hydrogen H_2 (Galama & Wijers 2001). The observed low detection rate of H_2 was therefore initially a puzzle, indicating an apparent lack of molecular gas in GRB-host absorption systems (e.g., Tumlinson et al. 2007). The observed H_2 deficiency was attributed to the typically low metallicities of the GRB-host absorbers observed with high-resolution spectrographs (Ledoux et al. 2009), or due to stronger UV radiation fields (Whalen et al. 2008; Chen et al. 2009). Since the absorption signatures of H_2 are the Lyman-Werner bands located bluewards of the Lyman-α line, the search for H_2 from the ground was also limited to $z \gtrsim 2$. Moreover, at $z \gtrsim 4$ the absorption features from H_2 become even more challenging to detect due to the increased Lyman forest line density. The first hint of molecular gas in GRB-host absorption systems came from the tentative detection of H_2 in GRB 060206 (Fynbo et al. 2006). However, it was not until the remarkable afterglow spectrum of GRB 080607 that the first unequivocal detection of H_2 in a GRB-host absorber was reported (Prochaska et al. 2009). The immense luminosity of this GRB (Perley et al. 2011) and the high H_2 column density made it possible to detect the absorption features from the UV Lyman-Werner bands, even in the low-resolution optical spectroscopy obtained of this GRB afterglow. Since then, six more H_2-bearing GRB absorbers have been securely detected (Krühler et al. 2013; D'Elia et al. 2014; Friis et al. 2015; Bolmer et al. 2019). Except for GRB 080607, all of these were observed with the more-sensitive, medium-resolution X-shooter spectrograph on the Very Large Telescope (VLT) as part of the extensive VLT/X-shooter GRB (XS-GRB) afterglow legacy survey (Selsing et al. 2019).

Star formation is driven and regulated by the availability of dense gas, which is expected to be in molecular form in the ISM (McKee & Ostriker 2007; Kennicutt & Evans 2012). Identifying and characterizing the molecular gas-phase is therefore vital to understand how stars are formed. At high redshifts, the presence of H_2 is most commonly inferred indirectly from other molecular gas tracers such as CO in emission-selected galaxy surveys (Solomon & Vanden Bout 2005; Carilli & Walter 2013), but its relation to H_2 at high-z and in the low-metallicity regime is still uncertain (Bolatto et al. 2013). Detecting the features from H_2, and other molecular gas species in absorption, therefore provides a unique window into the typical molecular gas content of high-z, star-forming galaxies. Recently, Heintz et al. (2019a) also showed that neutral atomic carbon (C I) could be used as a tracer of H_2 in GRB absorbers, suggesting that a relatively large fraction (~25%) of GRB sightlines intersect molecular clouds, also in the low-resolution spectroscopic GRB afterglow sample of Fynbo et al. (2009). Rarer molecules have also been detected in GRB afterglows, such as CH^+ in GRB 140506A (Fynbo et al. 2014) and vibrationally-excited H_2 (H_2^*) in GRBs 080607 and 120815A (Sheffer et al. 2009; Krühler et al. 2013). Identifying H_2-bearing clouds from these alternative molecular gas tracers might prove to be even more effective, since they can be detected even in low-resolution spectroscopy, and in very dust-obscured GRB afterglows at lower redshifts. Line emission from CO has also been detected in a small number of GRB host galaxies (Hatsukade et al. 2014; Stanway et al. 2015; Michałowski et al. 2016, 2018; Arabsalmani et al. 2018), providing an alternative way to establish the presence of molecular gas in the environments of GRBs.

Here we present the observations and detection of H_2 in the two host-galaxy absorption systems of GRB 181020A at $z = 2.938$ and GRB 190114A at $z = 3.376$. These two systems bring the total number of observed H_2-bearing GRB absorbers up to nine. Both afterglow spectra also show absorption features from C I and exhibit the third and fourth known detections of H_2^* in GRB-host absorption systems, respectively. The aim of this work is to explore the defining characteristics required for the H_2-bearing GRB absorbers to simultaneously probe C I and H_2^* and consequently quantify the use of the latter as alternative tracers of molecular-rich gas.

The paper is structured as follows. In Sect. 2, we present the observations of the two new GRB optical afterglows and the compiled sample of GRB-host absorbers with detected molecules. The absorption-line abundance analysis is described in Sect. 3, with specific focus on the identified molecular gas tracers. The results related to the defining characteristics of GRB-host absorption systems to show the presence of H_2, C I, and H_2^* is provided in Sect. 4. In Sect. 5, we explore the physical conditions of the molecular gas and discuss the potential implications of a significant dust bias affecting the H_2-detection probability in GRB-host absorbers. Finally, in Sect. 6 we present the conclusions of our work. Throughout the paper, errors denote the 1σ confidence level (unless stated otherwise) and column densities are expressed in units of cm^{-2}. We assume a standard flat cosmology with $H_0 = 67.8\,\mathrm{km\,s^{-1}\,Mpc^{-1}}$, $\Omega_\mathrm{m} = 0.308$ and $\Omega_\Lambda = 0.692$ (Planck Collaboration XIII 2016). Gas-phase abundances are expressed relative to the solar abundance values from Asplund et al. (2009), where $[\mathrm{X/Y}] = \log(N(\mathrm{X})/N(\mathrm{Y})) - \log(N(\mathrm{X})_\odot/N(\mathrm{Y})_\odot)$, following the recommendations by Lodders et al. (2009). Wavelengths are reported in vacuum.

2. Observations and sample description

The GRBs 181020A and 190114A were both detected by the Burst Alert Telescope (BAT; Barthelmy et al. 2005) onboard the

Table 1. Sample properties of the H_2- and/or C I-bearing XS-GRB absorbers.

GRB	z_{GRB}	log N(H I) (cm^{-2})	log $N(H_2)$ (cm^{-2})	log f_{H_2}	log N(C I) [a] (cm^{-2})	log N(CO) [a] (cm^{-2})	[X/H]	A_V (mag)
120119A	1.7288	22.44 ± 0.12	...	...	≳14.9	<15.7	−0.96 ± 0.28	1.02 ± 0.11
120327A	2.8143	22.07 ± 0.01	17.39 ± 0.13	−4.38 ± 0.14	<14.3	<15.3	−1.49 ± 0.03	<0.03
120815A	2.3582	22.09 ± 0.01	20.42 ± 0.08	−1.39 ± 0.09	14.24 ± 0.14	<15.0	−1.45 ± 0.03	0.19 ± 0.04
120909A	3.9290	21.82 ± 0.02	17.25 ± 0.23	−4.27 ± 0.25	<14.0	<14.2	−1.06 ± 0.12	0.16 ± 0.04
121024A	2.3005	21.78 ± 0.02	19.90 ± 0.17	−1.59 ± 0.18	13.91 ± 0.08	<14.4	−0.76 ± 0.06	0.26 ± 0.07
141109A	2.9940	22.18 ± 0.02	18.02 ± 0.12	−3.86 ± 0.14	<14.7	<15.9	−1.63 ± 0.06	0.11 ± 0.03
150403A	2.0571	21.73 ± 0.02	19.90 ± 0.14	−1.54 ± 0.15	≳14.3	<14.9	−1.04 ± 0.04	<0.13
180325A	2.2496	22.30 ± 0.14	...	...	≳14.5	<15.9	>−0.96	1.58 ± 0.12
181020A	2.9379	22.20 ± 0.05	20.40 ± 0.04	−1.51 ± 0.06	13.98 ± 0.05	<13.3	−1.57 ± 0.06	0.27 ± 0.02
190114A	3.3764	22.15 ± 0.05	19.44 ± 0.04	−2.40 ± 0.07	13.54 ± 0.08	<13.3	−1.23 ± 0.07	0.36 ± 0.02
080607	3.0363	22.70 ± 0.15	21.20 ± 0.20	−1.23 ± 0.24	>15.1 [b]	16.5 ± 0.3	>−0.2 [c]	2.58 ± 0.45

Notes. References for the measurements of the neutral and molecular gas-phase abundances and rest-frame A_V can be found in the appendix. [a]The measured 2σ upper or lower limits are provided for each GRB. [b]The lower limit on the total C I column density for GRB 080607 is inferred from the rest-frame equivalent width of C I (see Sect. 3.4). [c]The lower limit on the metallicity for GRB 080607 is derived from the [O/H] abundance following Prochaska et al. (2009).

Neil Gehrels Swift Observatory (*Swift* hereafter; Gehrels et al. 2004), as reported by Moss et al. (2018) and Laporte et al. (2019). We obtained optical to near-infrared (NIR) afterglow spectroscopy of both GRBs with the VLT/X-shooter instrument (Vernet et al. 2011). The spectrum of GRB 181020A was acquired (at the start of exposure) 5.7 h after the GRB with an acquisition magnitude of $R \sim 17.3$ mag (Fynbo et al. 2018). GRB 190114A was observed only 15 min after trigger with an acquisition magnitude of $R \sim 18.7$ mag, using the rapid-response mode (RRM; de Ugarte Postigo et al. 2019). The optical to NIR spectra of both GRBs were taken simultaneously in the ultraviolet (UVB), visual (VIS) and NIR arms of VLT/X-shooter with slit-widths of 1″.0, 0″.9, 0″.9, respectively. The observations were performed under excellent conditions with average seeing and airmasses of 1″.02, 1.25 (GRB 181020A) and 0″.47, 1.29 (GRB 190114A). Both spectra show very high signal-to-noise ratios (S/N), with S/N ≳ 30 at $\lambda_{obs} = 6700$ Å in the VIS arm spectra.

We reduced the afterglow spectra in a similar manner to that described in Selsing et al. (2019). The only update is that the reductions are based on the most recent version `v. 3.2.0` of the ESO X-shooter pipeline (Modigliani et al. 2010). The final extracted 1D spectra were moved to the barycentric frame of the Solar system in the post-processing and corrected for Galactic extinction along the line-of-sight to the bursts using the dust maps of Schlegel et al. (1998), but with the updated values from Schlafly & Finkbeiner (2011). We infer the delivered spectral resolution from the observed width of a set telluric absorption features in the VIS and NIR arms and rescale the nominal UVB arm resolution accordingly. To verify this, we also estimated the delivered resolution by fitting the spectral trace in the UVB arm with a Gaussian and derived the resolution from the full-width-at-half-maximum (FWHM) as FWHM $= 2\sqrt{2\ln 2}\sigma$, which yielded consistent results.

To complement the analysis of the molecular content and the physical conditions in GRBs 181020A and 190114A, we compile a sample of bursts selected from the VLT/X-shooter GRB (XS-GRB) afterglow legacy survey (Selsing et al. 2019) and the Stargate (PI: N. R. Tanvir) public data. This sample constitutes all GRBs observed with VLT/X-shooter to date that directly or indirectly show the presence of molecular gas. We have extracted all afterglows with known detections of molecular hydrogen (Krühler et al. 2013; D'Elia et al. 2014; Friis et al. 2015; Bolmer et al. 2019) and/or neutral atomic carbon (Zafar et al. 2018a; Heintz et al. 2019a), which has been found to be a good tracer of molecular gas (see e.g., Srianand et al. 2005; Noterdaeme et al. 2018). This collection is therefore not an unbiased representation of the GRB population as a whole, but rather a compilation of GRB afterglows where a determination of the relative gas content and the physical conditions in the molecular gas-phase is possible (see instead Bolmer et al. 2019 and Heintz et al. 2019a for statistical analyses of the presence of H_2 and C I in GRB afterglows). In total, we compiled ten XS-GRBs with H_2 and/or C I detected in absorption, listed in Table 1. Throughout the paper we will also compare our results to the only other GRB with a known detection of H_2 in absorption, GRB 080607 (Prochaska et al. 2009).

3. Data analysis

3.1. Atomic and molecular hydrogen

In the high S/N afterglow spectra of GRBs 181020A and 190114A, we clearly detect the absorption features from H_2 bluewards of the broad Lyα absorption trough (see Figs. 1 and 2). We measure the column densities of atomic and molecular hydrogen by simultaneously fitting the absorption lines from H I and the H_2 Lyman-Werner bands following the same routine as described in Bolmer et al. (2019). Here, the absorption lines are modelled with Voigt profiles and fit simultaneously with the continuum flux of the GRB afterglow. The absorption lines are then convolved with the delivered spectral resolution in the UVB arm spectra of $\mathcal{R} = 6750$ (or 44.4 km s^{-1}, GRB 181020A) and $\mathcal{R} = 7020$ (or 42.7 km s^{-1}, GRB 190114A). The fitting routine is a custom-made `Python` module, based on the Markov chain Monte Carlo (MCMC) Bayesian inference library `PyMC 2.3.7` (see Bolmer et al. 2019, for further details). For GRB 181020A we derive a total H I column density of log N(H I) = 22.20 ± 0.05, consistent with Tanvir et al. (2019), at a redshift of $z = 2.938$, and for GRB 190114A we derive log N(H I) = 22.15 ± 0.05 at $z = 3.376$. In both afterglow spectra, we detect all the rotational levels of H_2 up to $J = 3$ (see Sect. 5.1 for further discussion on the $J \geq 4$ levels).

To determine the H_2 abundances we tied the redshifts and b-parameters in the fit for all the detected rotational levels, and

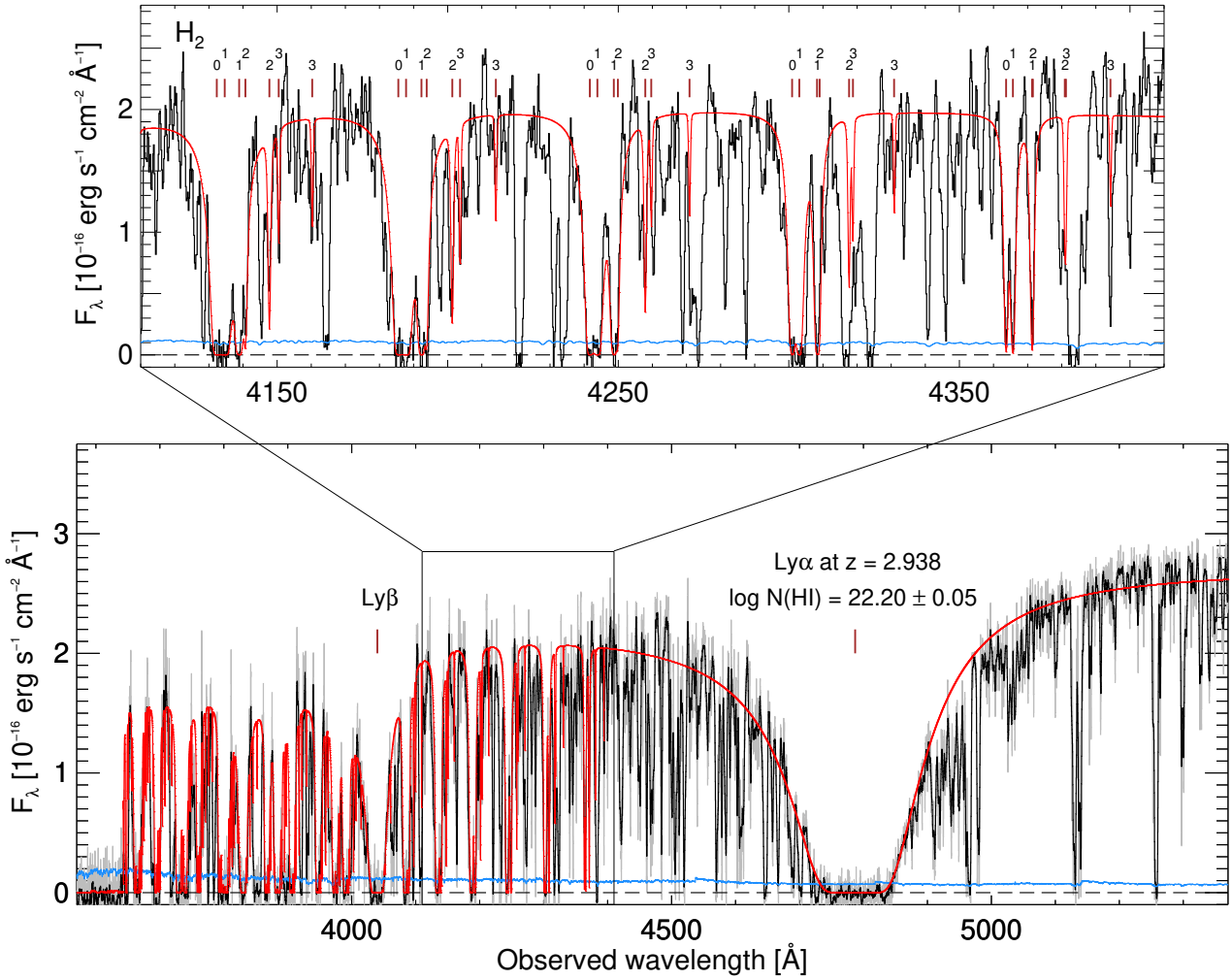

Fig. 1. VLT/X-shooter UVB arm spectrum of GRB 181020A. The absorption features from the H I Lyα, Lyβ and H_2 Lyman-Werner band line transitions are clearly shown. The raw spectrum is shown in gray with the associated error spectrum in blue. A binned version of the spectrum is overplotted in black. A synthetic spectrum of the best fit model to H I and H_2 is shown as the solid red line and the Lyα and Lyβ absorption features are marked at the observed redshift of $z = 2.938$. *Top panel*: a zoom-in of a subset of the most constraining Lyman-Werner band line transitions from molecular hydrogen. The redshifted wavelengths of the strongest rotational levels $J = 0, 1, 2, 3$ are marked above each line.

find a best fit assuming a single absorption component. For GRB 181020A we measure column densities of $\log N(H_2, J = 0, 1, 2, 3) = 20.14 \pm 0.05$, 20.06 ± 0.03, 18.38 ± 0.21, and 18.05 ± 0.25, and thus a total H_2 column density of $\log N(H_2) = 20.40 \pm 0.04$ with a broadening parameter of $b = 3 \pm 2\,\mathrm{km\,s^{-1}}$. For GRB 190114A we derive $\log N(H_2, J = 0, 1, 2, 3) = 19.28 \pm 0.05$, 18.90 ± 0.03, 17.92 ± 0.02, and 17.62 ± 0.25 resulting in a total H_2 column density of $\log N(H_2) = 19.44 \pm 0.04$ with a broadening parameter of $b = 2 \pm 1\,\mathrm{km\,s^{-1}}$. Since the lowest rotational levels ($J = 0, 1$) of H_2 are damped in both cases, the determination of the column density in these levels is not sensitive to b. Because these transitions dominate the H_2 content, the estimates of the total $N(H_2)$ in both cases should be robust. While both fits are consistent with a single absorption component, we caution that at this resolution the observed line profiles might be comprised of a number of narrower features such that inferred H_2 abundances represent the integrated H_2 column density. Synthetic spectra of the best-fit models of H I and H_2 in GRBs 181020A and 190114A are shown in Figs. 1 and 2, overplotted on the UVB arm spectra.

For the remaining GRBs in our sample, column densities of atomic and molecular hydrogen have been derived previously in the literature. Throughout the paper, we report the column densities measured by Bolmer et al. (2019) to be consistent within the sample, except for GRBs 120119A and 180325A, where we adopt the derived H I column densities from Wiseman et al. (2017) and Zafar et al. (2018a), respectively (since they were not part of the statistical sample of Bolmer et al. 2019). For a more detailed analysis of some of the individual systems, see the dedicated single-burst papers (e.g., for GRB 120327A: D'Elia et al. 2014; GRB 120815A: Krühler et al. 2013; and GRB 121024A: Friis et al. 2015).

3.2. Gas-phase abundances and dust extinction

In addition to the H I and H_2 transition lines we detect a wealth of low-ionization metal absorption features in the afterglow spectra of GRBs 181020A and 190114A. To determine the gas-phase abundances, we again fit a range of Voigt profiles to a set of carefully-selected absorption lines, free of tellurics or unrelated blends. The host absorber toward GRB 181020A shows a complex velocity structure with five identified strong absorption components (see Fig. A.1 for a few examples of lines showing this structure). The absorption line profiles in the host absorber

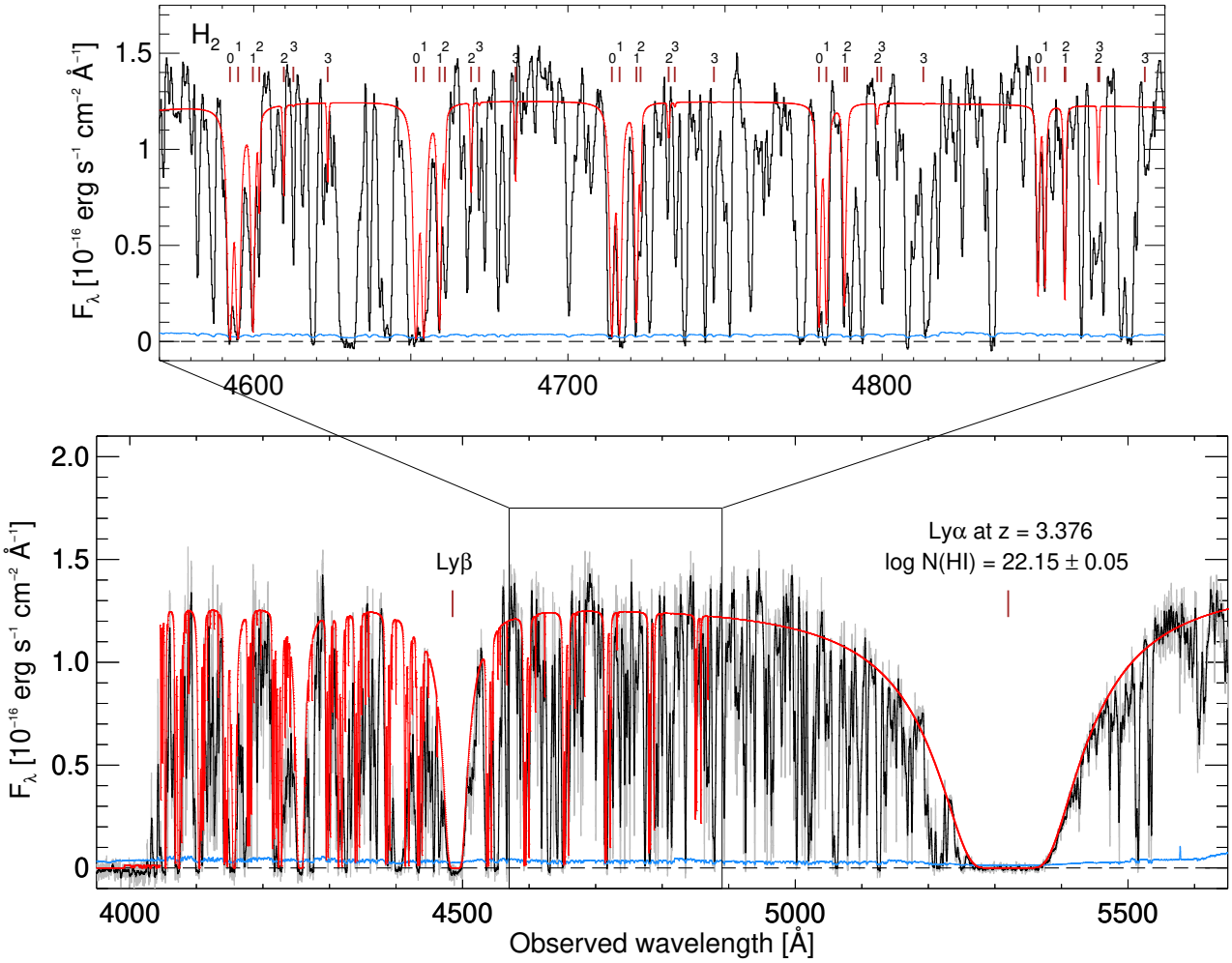

Fig. 2. Same as Fig. 1 but for GRB 190114A at $z = 3.376$.

of GRB 190114A show a simpler velocity structure, with one dominant component and an additional weaker component at $\delta v = -40\,\mathrm{km\,s^{-1}}$ (see Fig. A.2). We constrain the column densities from the weakest transitions of each element by fixing the velocity structure to that observed in the strongest line complexes.

For GRB 181020A we derive column densities of $\log N(\mathrm{Fe}) = 15.47 \pm 0.01$, $\log N(\mathrm{Zn}) = 13.19 \pm 0.03$, and $\log N(\mathrm{Cr}) = 14.16 \pm 0.02$, resulting in a gas-phase metallicity of $[\mathrm{Zn/H}] = -1.57 \pm 0.06$ and dust-depletion $[\mathrm{Zn/Fe}] = 0.67 \pm 0.03$. Following De Cia et al. (2016) we compute a dust-corrected metallicity, $[\mathrm{M/H}] = [\mathrm{X/H}] - \delta_X$ (where δ_X is inferred from the iron-to-zinc depletion), of $[\mathrm{M/H}] = -1.39 \pm 0.05$. For GRB 190114A we measure gas-phase abundances of $\log N(\mathrm{Fe}) = 15.37 \pm 0.04$, $\log N(\mathrm{Zn}) = 13.48 \pm 0.04$, and $\log N(\mathrm{Cr}) = 13.95 \pm 0.05$, resulting in a metallicity of $[\mathrm{Zn/H}] = -1.23 \pm 0.07$ and dust-depletion $[\mathrm{Zn/Fe}] = 1.06 \pm 0.08$. This yields a dust-corrected metallicity of $[\mathrm{M/H}] = -0.94 \pm 0.06$. The gas-phase abundances of GRBs 181020A and 190114A, together with literature values for the other GRBs in our sample, are summarized in Table 1. Again, we adopt the values derived by Bolmer et al. (2019) for the majority of the sample, except for GRBs 120119A and 180325A (see the appendix for details).

The visual extinction A_V along the line-of-sight to both GRBs were measured following the same approach as in Heintz et al. (2019a). Briefly, this assumes a simple underlying power-law shape of the afterglow spectrum, with a wavelength-dependent extinction coefficient A_λ imposed as $F_{\mathrm{obs}} = F_\lambda \times 10^{-0.4A_\lambda}$ where $F_\lambda = \lambda^{-\beta}$. We then fit the underlying power-law slope and extinction coefficient simultaneously. Using the extinction-curve parametrization from Gordon et al. (2003), we find a best fit with an SMC-like extinction curve in both GRB sightlines and measure $A_V = 0.27 \pm 0.02$ mag (for GRB 181020A, see Fig. A.3) and $A_V = 0.36 \pm 0.02$ mag (for GRB 190114A, see Fig. A.4). We do not find any indication of the 2175 Å dust extinction bump in either of the bursts, so we derive upper limits on the bump strength, $A_{\mathrm{bump}} = \pi c_3/(2\,\gamma\,R_V) \times A_V$, of $A_{\mathrm{bump}} < 0.07$ mag (GRB 181020A) and $A_{\mathrm{bump}} < 0.09$ mag (GRB 190114A) at 3σ. The measured visual extinction along the line-of-sight toward GRBs 181020A and 190114A, together with literature values for the other GRBs in our sample, are again summarized in Table 1.

3.3. Vibrationally-excited molecular hydrogen

After clearly establishing the presence of H_2 in both the afterglow spectra of GRBs 181020A and 190114A, we searched for the so-far rarely detected absorption features from vibrationally-excited H_2 (H_2^*) (see Bolmer 2019). The vibrationally-excited levels of H_2 are expected to be populated by UV pumping from the GRB afterglow (Draine 2000), but to date they have only been securely detected in two afterglow spectra,

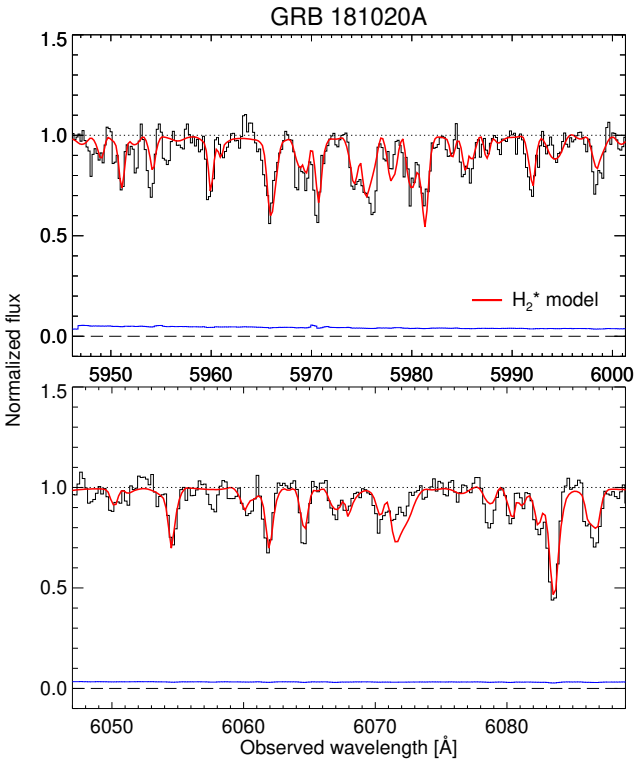

Fig. 3. Normalized VLT/X-shooter VIS arm spectrum of GRB 181020A showing regions encompassing a subset of the strongest H_2^* lines. The solid black lines show the data, the blue lines the associated error and the red lines the best-fit model.

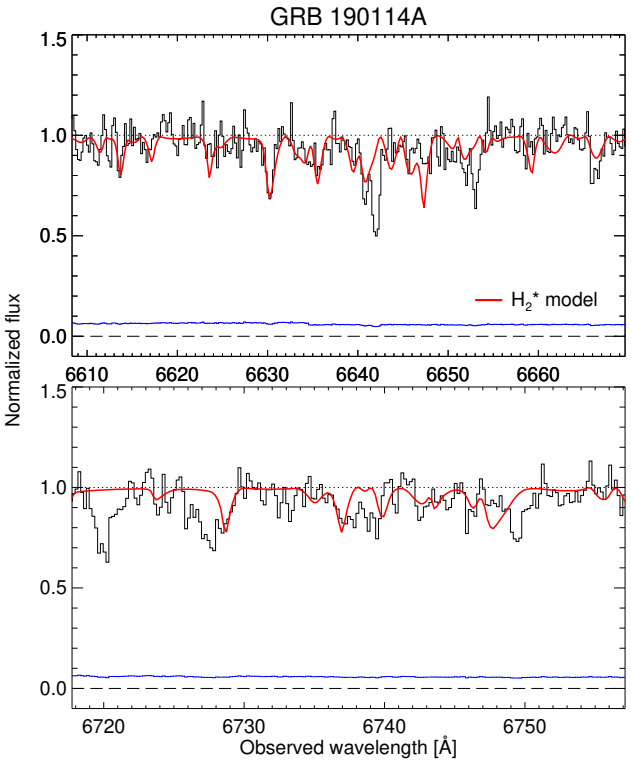

Fig. 4. Same as Fig. 3 but for GRB 190114A.

those of GRB 080607 (Sheffer et al. 2009) and GRB 120815A (Krühler et al. 2013). We performed the search by using the synthetic spectrum from Draine & Hao (2002), downgraded to the resolution of the given arm (in both cases the VIS arm, with $\mathcal{R} \sim 11\,000$). In the fit, we included any intervening metal lines and matched the model to the whole spectrum redwards of Lyα up until 1650 Å (rest frame). We use PyMC (as described in Sect. 3.1) to sample the posteriors of the optical depth τ and the redshift of the H_2^* absorption lines, as well as the continuum flux.

We clearly detect H_2^* in both afterglow spectra of GRBs 181020A and 190114A. Even including the uncertainty on the continuum flux due to the wealth of absorption features from H_2^*, we consider the detections highly significant due to the overall excellent match with the data and fit to several strong individual lines. For GRB 181020A we derive a column density of $\log N(H_2^*) = 16.28 \pm 0.05$, with the best-fit model shown in Fig. 3. For GRB 190114A, we measure $\log N(H_2^*) = 16.13 \pm 0.13$, with the best-fit model shown in Fig. 4. We caution that small deviations of the spectrum from the model are expected due to the different initial conditions, such as the luminosity of the GRB afterglow, dust content and shielding, and distance to the absorbing cloud (Krühler et al. 2013). A detailed modelling of the lines will be provided in a follow-up paper to constrain the origin of H_2^* (Bolmer et al., in prep.). The H_2^* column densities of GRBs 181020A and 190114A are of the same order as the one observed in GRB 120815A, all being roughly an order of magnitude lower than what was observed in GRB 080607 (Sheffer et al. 2009). For the other GRBs in our sample, we are able to place upper limits on the H_2^* column density typically 5−10 times lower than those observed in GRBs 120815A, 181020A and 190114A using the same routine (see also Bolmer et al. 2019).

3.4. Neutral atomic carbon

In addition to H_2 and H_2^*, we also detect absorption features from C I in both afterglow spectra of GRBs 181020A and 190114A, which has been found to be an efficient tracer of molecule-rich gas. Recently, Heintz et al. (2019a) surveyed C I in a large sample of GRB afterglows observed both with low- and medium-resolution spectrographs (including some of the XS-GRBs in the sample presented here). To be consistent with the part of the sample observed with low-resolution spectrographs (where meaningful column densities cannot be derived) and with the survey for C I in high-z quasar absorbers (Ledoux et al. 2015), only the total C I equivalent widths were measured in that study. In this work, we attempt to derive the C I column densities for all the XS-GRBs, including the sample studied in Heintz et al. (2019a), by fitting a set of Voigt profiles to the relevant transitions. For this, we used the `Python` module `VoigtFit`[1] (Krogager 2018), where the absorption line profiles again have been convolved with the delivered instrumental resolution.

The three fine-structure levels ($J = 0, 1, 2$) of neutral carbon's ground-state triplet, here denoted C I, C I*, C I**, respectively, are all resolved in the VLT/X-shooter spectra (see also e.g., Krogager et al. 2016; Ranjan et al. 2018). We simultaneously fit the three fine-structure levels, assuming a single component and by tying the Doppler parameters and redshifts. This is based on the assumption that the excited fine-structure levels (C I* and C I**) share the same physical origin as the ground level (C I) and therefore follow the same kinematic structure.

For GRB 181020A we derive column densities of $\log N$(C I, C I*, C I**) = 12.82 ± 0.13, 13.45 ± 0.05, and 13.78 ± 0.07, and thus a total C I column density of $\log N(\mathrm{C\,I}) = 13.98 \pm 0.05$ with a best-fit broadening parameter of $b = 3.9 \pm 0.8\,\mathrm{km\,s^{-1}}$.

[1] https://github.com/jkrogager/VoigtFit

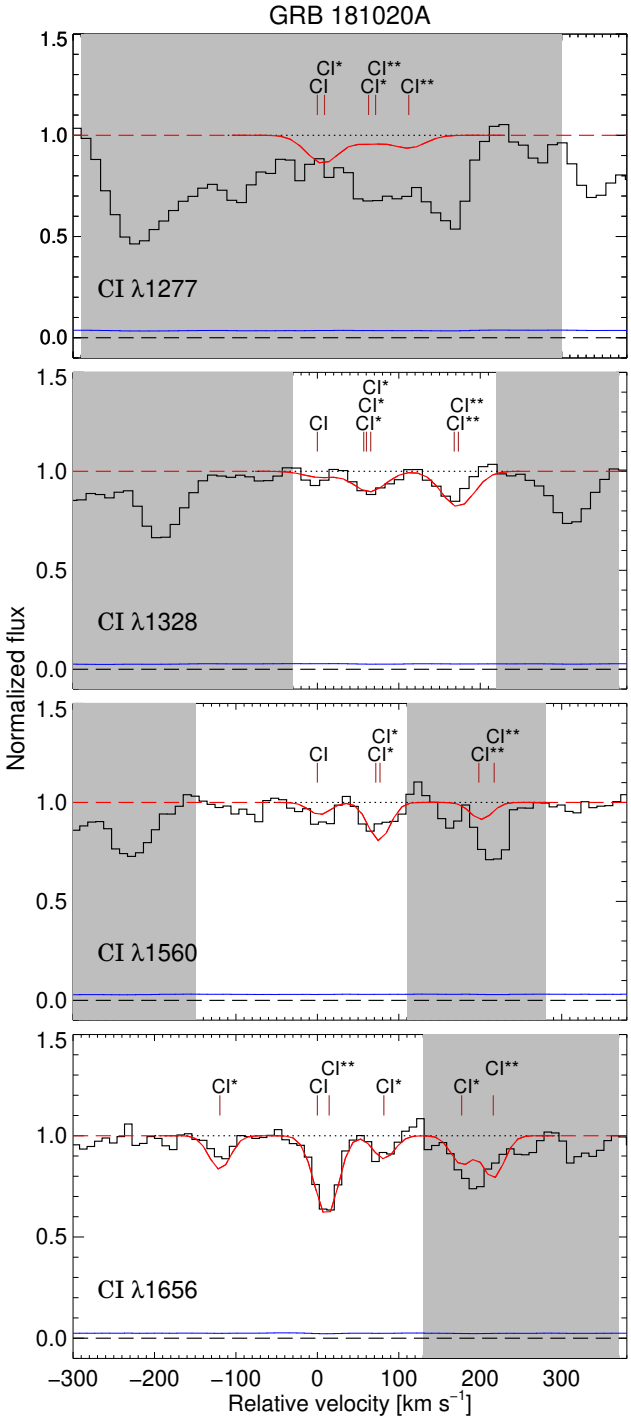

Fig. 5. Normalized VLT/X-shooter VIS arm spectrum of GRB 181020A in velocity space, centered on the ground-state transition of C I at z = 2.93786. Again, the solid black lines show the data, the blue lines the associated error and the red lines the best-fit model. The C I ground-state and excited line transitions are marked above each of the absorption profiles. Gray shaded regions were ignored in the fit.

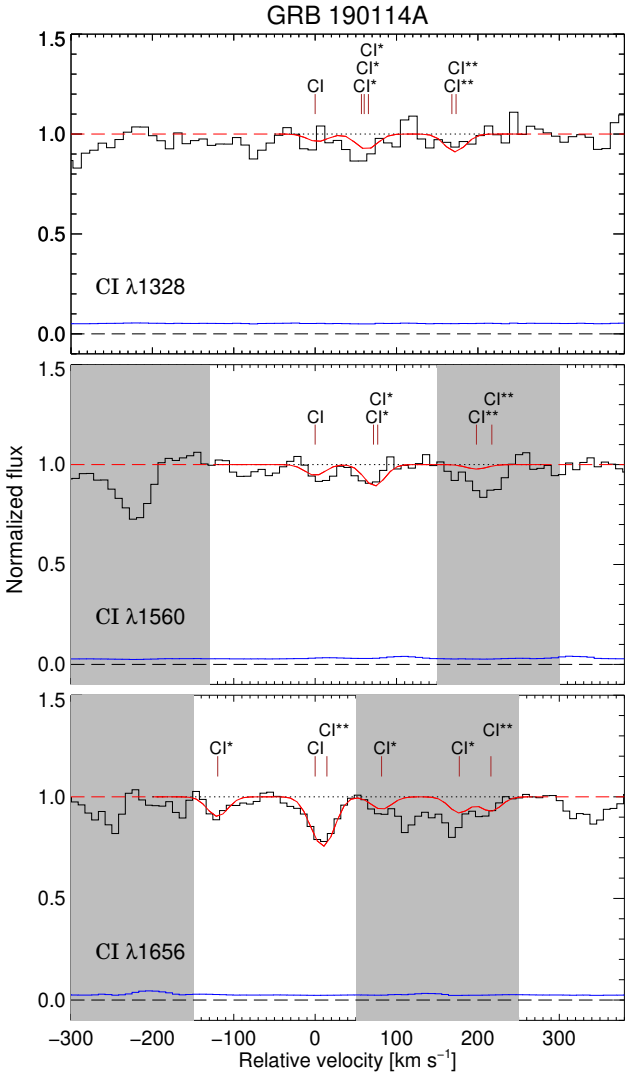

Fig. 6. Same as Fig. 5 but for GRB 190114A and with a fixed value of $b = 5\,\mathrm{km\,s^{-1}}$, centered on $z = 3.37638$.

The best-fit Voigt profiles are shown in Fig. 5. We only detect a single absorption component across the four line complexes so we fixed this in the fit and masked out any unrelated or blended features. The fit was only constrained by the C I $\lambda\lambda\lambda$ 1328,1560,1656 transition lines, since the C I λ 1277 line is significantly blended with tellurics and unrelated absorption features. For GRB 190114A we compute relative C I abundances of $\log N(\mathrm{C\,I}, \mathrm{C\,I^*}, \mathrm{C\,I^{**}}) = 12.79 \pm 0.15$, 13.12 ± 0.15, and 13.19 ± 0.11, and thus a total C I column density of $\log N(\mathrm{C\,I}) = 13.54 \pm 0.08$. In this case, we fixed the broadening parameter to $b = 5\,\mathrm{km\,s^{-1}}$, since the fit could not converge on a realistic b-value due to significant blending of several of the lines. The best-fit model with fixed $b = 5\,\mathrm{km\,s^{-1}}$ is shown in Fig. 6. It was only possible to perform the fit on the C I $\lambda\lambda\lambda$ 1328,1560,1656 line transitions, since the C I λ 1277 line is located in the overlap region between the UVB and VIS arm. We only detect a single absorption component across the three line complexes in this case as well, so we fixed this in the fit and masked out any unrelated or blended features. The line profiles seem to exclude values of $b \gtrsim 5\,\mathrm{km\,s^{-1}}$ and $b \lesssim 3\,\mathrm{km\,s^{-1}}$, both when considering the line widths and the relative optical depths.

For the other GRBs in our sample where C I is detected, the derived column densities are listed in Table 1. Here, we also provide upper limits for the H_2-bearing GRB absorbers which show non-detections of C I assuming $b = 2\,\mathrm{km\,s^{-1}}$ to be consistent with the limits derived for the abundance of CO (Bolmer et al. 2019). In the appendix, a more detailed description of the fit performed for each individual GRB is given, together with plots showing the best-fit Voigt profiles and tables listing the derived column densities for each of the excited states and Doppler parameters. For the bursts where C I is most

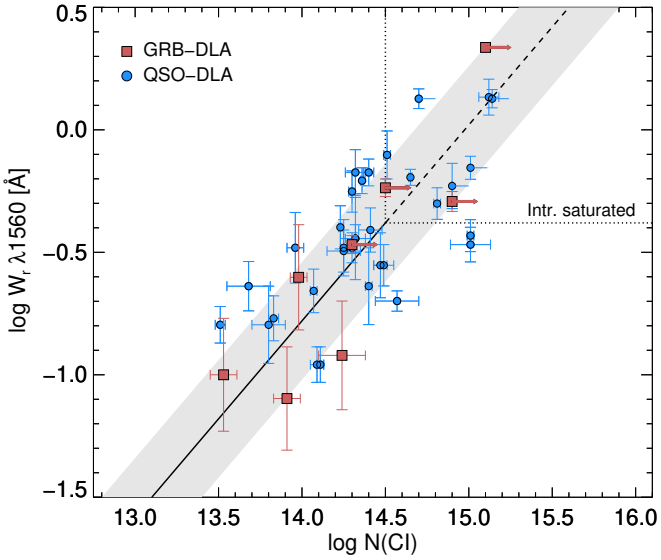

Fig. 7. C I λ 1560 rest-frame equivalent width as a function of total C I column density. Red squares denote GRB C I absorbers from this work. Blue dots show the C I-selected quasar absorbers from Ledoux et al. (2015), for which Noterdaeme et al. (2018) measured the total N(C I) from high-resolution spectroscopy. The black line shows the best linear fit where the σ = 0.3 dex scatter is shown by the gray-shaded region. The approximate column density (and equivalent width) at which the intrinsic C I lines saturate are marked by the dotted lines.

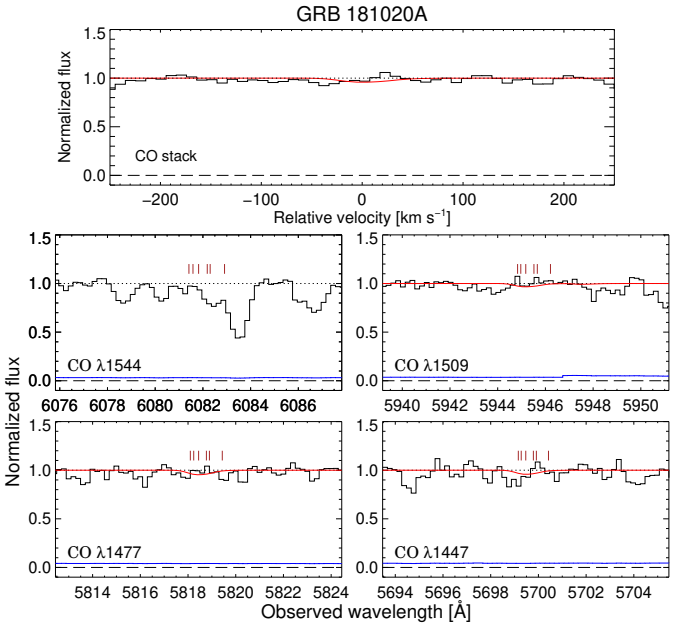

Fig. 8. Normalized VLT/X-shooter VIS arm spectrum of GRB 181020A showing the regions where the strongest CO band absorption lines are expected including a stacked spectrum (excluding CO λ 1544). Again, the solid black lines show the data and the blue lines the associated error. Line profiles showing the derived upper limits on N(CO) are overplotted in red.

prominent (GRBs 120119A, 150403A, and 180325A) we only provide the 2σ lower limit on the total column density in Table 1 since the lines are intrinsically saturated. For GRBs 120815A, 121024A, 181020A, and 190114A we provide the derived total C I column densities in Table 1. We caution, however, that since we are not able to distinguish additional narrow absorption components at the observed spectral resolution, these values should in principle only represent the lower limits on N(C I) due to the possible effect of "hidden" saturation (e.g., Prochaska 2006). Nevertheless, the inferred b-parameters and column densities are consistent with similar C I absorption systems observed toward quasars (e.g., Srianand et al. 2005).

For GRB 080607 (Prochaska et al. 2009) we derive a lower limit on the total C I column density based on the equivalent width measurements from Fynbo et al. (2009) of log N(C I) > 15.1. To estimate this abundance more precisely, we compare the C I equivalent widths derived by Ledoux et al. (2015) for the quasar C I absorbers with the total column densities measured in the high-resolution spectra of the same absorption systems (Noterdaeme et al. 2018). From a linear fit to the data (excluding the systems with log N(C I) > 14.5, at which point the line profiles become saturated) we find a correlation of

$$\log W_{\rm r}(\lambda 1560) = 0.8 \log N(\mathrm{C\,I}) - 11.98 \quad (1)$$

with a scatter of σ = 0.3 dex (see Fig. 7). This relation simply represents the evolution of equivalent width for absorption lines located on the linear part of the curve-of-growth. However, since all three fine-structure line transitions of C I contribute to the measured equivalent width in low-resolution spectra, this empirical relation provides a method to infer the total C I column density without considering the relative contributions from the three fine-structure levels. For GRB 080607, we then estimate log N(C I) = 15.4 ± 0.3 based on this relation, consistent with the lower limit inferred from the equivalent width. To be conservative, we will only consider the lower limit for this GRB throughout the paper. We also note that the C I equivalent widths and column densities derived for the rest of the GRB C I absorbers studied here are also consistent with the correlation observed in quasar absorbers. This linear relation therefore provides a robust way of constraining the total C I column density for non-saturated lines for C I absorption systems observed with low-resolution spectra. The observed scatter of σ = 0.3 dex is likely dominated by errors, but could also reflect the varying degree of the populations in the excited fine-structure levels relative to the ground-state.

3.5. Carbon monoxide

We also searched the afterglow spectra of GRBs 181020A and 190114A for absorption features originating from carbon monoxide (CO). To date, the only detection of CO absorption lines in a GRB afterglow is toward the remarkable burst GRB 080607 (Prochaska et al. 2009). Recently, Bolmer et al. (2019) derived upper limits on the CO column density for all the H_2-bearing GRB-DLAs examined in this study (except for GRBs 181020A and 190114A). We also note that de Ugarte Postigo et al. (2018) searched for CO absorption both in VLT/X-shooter and ALMA spectroscopy of GRB 161023A but were also only able to determine upper limits (this GRB did not show features from H_2 down to deep limits, however). In Figs. 8 and 9 we show the region of the spectra where the strongest CO band absorption lines should be located in GRBs 181020A and 190114A, respectively, and a stack of all line complexes (excluding CO λ 1544 in both cases due to blending). We do not detect any evidence of CO in either of the GRB afterglow spectra. To measure the upper limits on N(CO) in GRBs 181020A and 190114A we follow the same approach as Noterdaeme et al. (2018) and compute global (i.e., from the stacked spectra) χ^2 values for a range of column densities, where the 3σ upper limit

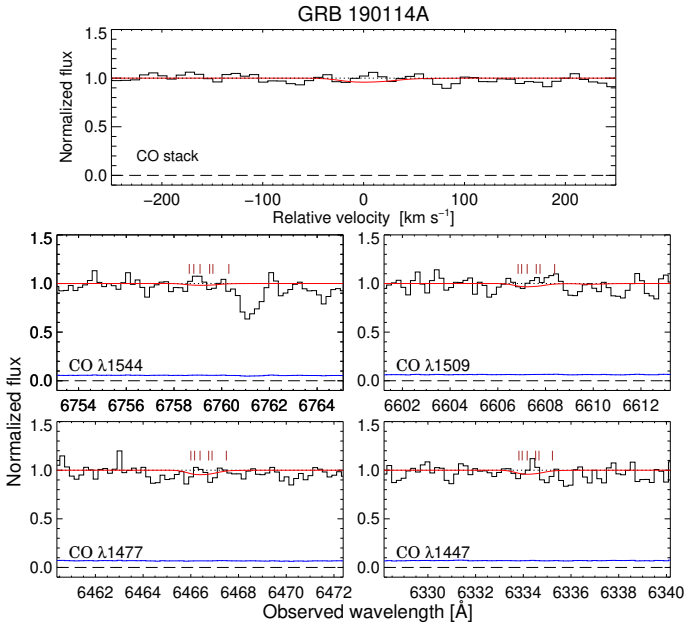

Fig. 9. Same as Fig. 8 but for GRB 190114A.

corresponds to the column density where the χ^2 is 9. This limit is naturally more stringent than inferred locally for each band individually. For both GRBs 181020A and 190114A we derive 3σ upper limits of $\log N(\mathrm{CO}) < 13.3$. The individual and stacked CO line profiles showing the upper limits on N(CO) are overplotted in red in Figs. 8 and 9. To be complete, we derive additional limits for GRBs 120119A and 180325A (which were not part of the study of Bolmer et al. 2019). A summary of the resulting upper limits on the abundance of CO for the GRBs studied in this work is provided in Table 1.

4. Results

4.1. Classification of the molecular gas-phase in GRB hosts

The total set of H I, H_2, C I and CO column densities, the derived gas-phase metallicities, and visual extinctions, A_V, for the GRBs in our sample is provided in Table 1. All the GRB absorption systems show prominent amounts of neutral atomic hydrogen ($N(\mathrm{H\,I}) > 5 \times 10^{21}$ cm^{-2}), comparable to the H I content of extremely strong quasar DLAs (ES-DLAs, Noterdaeme et al. 2014, 2015). This further supports the hypothesis that ES-DLAs probe the neutral gas disc of intervening galaxies in quasar sightlines, similar to GRB-selected absorption systems. We observe H_2 column densities in the (large) range $N(H_2) = 10^{17.2}$ to $10^{20.5}$ cm^{-2}, which yield integrated molecular fractions, $f_{H_2} = 2N(H_2)/(2N(H_2) + N(\mathrm{H\,I}))$, between $f_{H_2} = 10^{-4.4}$ and $10^{-1.4}$. We caution that in the core of the cloud where H_2 (and C I) is detected, the molecular fraction is likely higher than the integrated value (Balashev et al. 2015) since a fraction of the atomic hydrogen is located in the "warm" neutral medium (WNM) of the ISM.

To classify the molecular gas-phase observed in GRB hosts, we follow the definition of Burgh et al. (2010). Here, diffuse molecular clouds are defined by having $N(\mathrm{C\,I})/N(\mathrm{CO}) > 1$, where values below are found to trace translucent molecular gas (i.e., the transition between diffuse and dark molecular clouds, see e.g., Snow & McCall 2006). In Fig. 10 we plot the H_2 measurements and the upper limits on the CO column densities as a function of the total C I column densities for the GRB

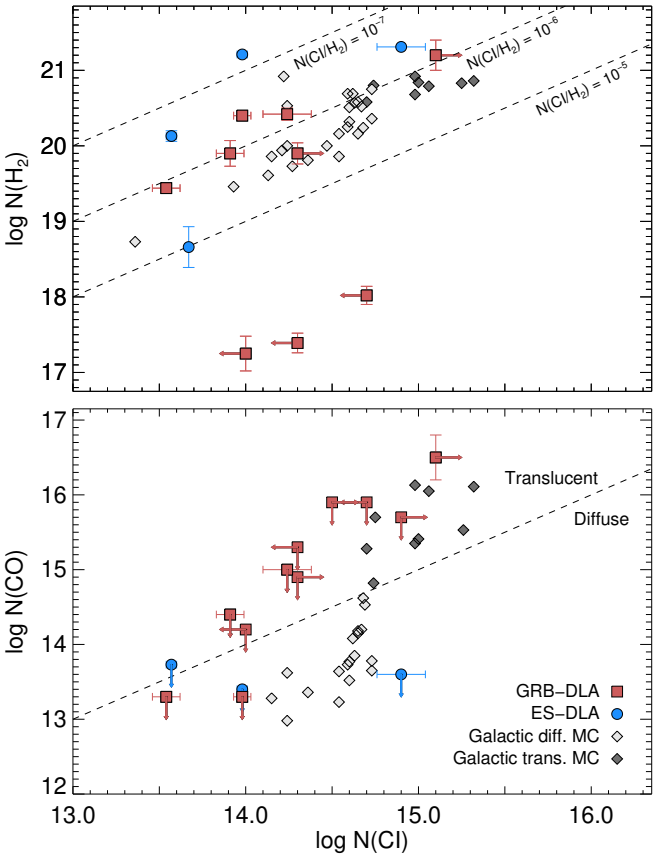

Fig. 10. H_2 (*top panel*) and CO (*bottom panel*) vs C I column densities for the GRB molecular gas absorbers studied in this paper. For comparison, we also show a compiled sample of ES-DLAs with a secure detection of H_2 from Guimarães et al. (2012), Noterdaeme et al. (2015), Balashev et al. (2017), Ranjan et al. (2018), and selected sightlines through diffuse and translucent molecular clouds in the Milky Way (from Burgh et al. 2010). *Top panel*: a set of constant C I-to-H_2 abundance ratios are shown for guidance. In the bottom panel, the transition region between diffuse and translucent molecular clouds at $N(\mathrm{C\,I})/N(\mathrm{CO}) = 1$ is shown as well.

molecular gas absorbers in our sample. For comparison, we also show a small sample of ES-DLAs with a secure detection of H_2 (compiled from Guimarães et al. 2012; Noterdaeme et al. 2015; Balashev et al. 2017; Ranjan et al. 2018), in addition to various diffuse and translucent molecular clouds in Galactic sightlines (from Burgh et al. 2010). We are not able to classify the XS-GRB molecular gas absorption systems studied here based on this classification scheme, but the typical abundance ratios of $N(\mathrm{C\,I})/N(H_2) \approx 10^{-6}$ and the low total $N(\mathrm{C\,I}) < 14.5$ column densities are consistent with originating from diffuse molecular clouds. This is also supported by their CO/H_2 column density ratios and the molecular-hydrogen fractions of the systems (Bolmer et al. 2019). The only exception is the host absorption system of GRB 080607 with a relative abundance ratio of $\log N(\mathrm{CO}/H_2) = -4.7 \pm 0.4$, consistent with originating from a translucent molecular cloud (also defined as having CO/H_2 $>10^{-6}$; Burgh et al. 2010).

We note that in order to observe CO at a detectable level ($\log N(\mathrm{CO}) \gtrsim 14$), either an H_2 column density of $\log N(H_2) > 20.5$ is required following the CO to H_2 correlation plot by Sheffer et al. (2008) or a C I column density of $\log N(\mathrm{C\,I}) > 15$ (for typical diffuse molecular clouds), which would explain the non-detection of CO in the XS-GRB absorbers. The lower-than-solar metallicity of GRB absorbers would also result in an even

lower expected CO-to-H_2 abundance ratio, further decreasing their detection probability.

Translucent molecular clouds can also be classified by having $A_V > 1$ mag (Snow & McCall 2006, see also Sect. 4.4). In our sample, only the GRBs 120119A and 180325A (except for GRB 080607) have dust columns consistent with this value. Unfortunately, GRB 120119A is at too low a redshift for the Lyman-Werner bands to enter the observable UV range. For GRB 180325A, the region of the spectrum where the potential Lyman-Werner absorption bands are present is completely suppressed by the high visual extinction (Zafar et al. 2018a; Bolmer et al. 2019).

4.2. Presence of vibrationally-excited H_2

Identifying the absorption features from H_2^* opens a potential route to establish the presence of molecular hydrogen in cases where a direct search for H_2 is not possible. Typical limitations are bursts being at too low redshifts ($z \lesssim 2$) to not cover the wavelength range bluewards of Lyα or significant blending of the Lyman-Werner bands with the Lyα forest in low-resolution spectroscopy (Krühler et al. 2013; Bolmer 2019). Fully exploiting H_2^* as a molecular gas tracer, however, requires a good understanding of the observable characteristics of the H_2^*-bearing GRB absorbers. In Fig. 11 we show the positive detections and column densities of H_2^* in GRBs 080607, 120815A, 181020A and 190114A as a function of the H_2 column density and molecular-hydrogen fraction f_{H_2}. Except for GRB 190114A, H_2^* is only detected in GRB absorbers with $\log N(H_2) \gtrsim 20$ and $f_{H_2} > 0.03$. The high S/N afterglow spectrum of GRB 190114A could explain the detection of H_2^* even though the absorber has a ~10 times lower H_2 column density and molecular-hydrogen fraction than the other bursts with positive H_2^* detections. We note though that GRBs 121024A and 150403A, both with H_2 column densities and molecular fractions in the same range as GRBs 080607, 120815A, and 181020A, do not show any presence of H_2^* down to $\log N(H_2^*) < 15.7$, which is ~5 times less abundant than in the GRB-DLAs 120815A, 181020A, and 190114A.

We additionally examine the dependence on the intrinsic burst luminosity for the detection probability of H_2^*, representing the intensity or amount of photons from the GRB producing the excitation of H_2. We compute the GRB energy output in the observed 15–150 keV *Swift*-BAT band as $E_{BAT} = F_\gamma\, 4\pi\, d_L^2\, (1+z)^{-1}$ following Lien et al. (2016), where F_γ is the observed BAT fluence in the 15–150 keV band and d_L is the luminosity distance to the bursts at the given redshift. While GRBs 080607 and 181020A are among the most luminous bursts at $z \sim 3$ with $E_{BAT} > 2 \times 10^{53}$ erg (see e.g., Selsing et al. 2019), GRBs 120815A and 190114A are part of the faintest *Swift*-detected population of bursts at their respective redshifts.

This preliminary analysis seems to indicate that the detection probability of H_2^* is likely related to several intrinsic parameters such as GRB luminosity, distance from the bursts to the absorbing molecular gas and the observational difficulty to detect H_2^* with a typical low relative abundance compared to H_2 of $N(H_2^*)/N(H_2) \sim 10^{-4}$. This will be explored further in a follow-up paper (Bolmer et al., in prep.).

4.3. Detecting neutral atomic carbon in GRB H_2 absorbers

Molecular hydrogen observed in absorption is typically associated with C I in high-redshift QSO-DLA systems (Ge & Bechtold 1999; Srianand et al. 2005). C I-selected quasar absorbers (Ledoux et al. 2015) have also been shown to always

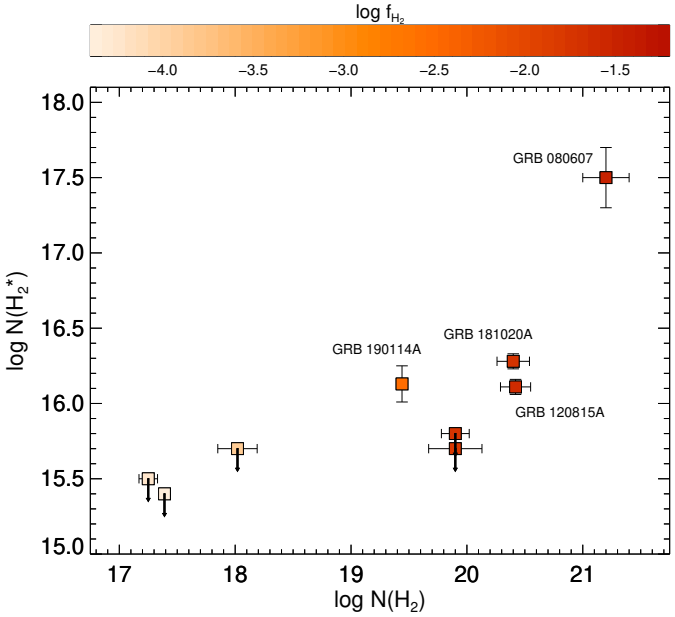

Fig. 11. Vibrationally-excited H_2 (H_2^*) vs. column densities of H_2 in the H_2-bearing GRB absorbers, color-coded as a function of the measured molecular fraction f_{H_2}. The four GRB systems with positive detections of H_2^* are marked individually.

contain H_2 (Noterdaeme et al. 2018). However, C I is not ubiquitous in all H_2-bearing systems. The incidence rate of H_2 in quasar DLAs is of the order ≈5–10% (Ledoux et al. 2003; Noterdaeme et al. 2008; Jorgenson et al. 2014; Balashev et al. 2014; Balashev & Noterdaeme 2018), whereas strong C I absorption features are only found in ≈1% of quasar absorbers (Ledoux et al. 2015). In this study, we consistently find that H_2 is always coincident with C I when the Lyman-Werner features are observable (excluding GRBs 120119A and 180325A) in GRB-host absorbers. On the other hand, C I is not detected in all the H_2-bearing GRB-host absorbers (as is the case for GRBs 120327A, 120909A, and 141109A), down to similar limits as derived for the bursts with detections of C I.

One explanation could be that H_2-bearing absorbers with low metallicities consequently have less prominent amounts of carbon, below the typical detection threshold. Another possibility is that C I has not been formed significantly in H_2 absorbers with low molecular fractions which consequently provide less shielding, such that the line-of-sight only intersects the outermost, more diffuse regions of the cloud. To explore the conditions for C I to be detected in the molecular gas-phase further, we examine the molecular-hydrogen fraction, f_{H_2}, of the H_2-bearing GRB absorbers as a function of metallicity in Fig. 12. For comparison, we overplot the sample of quasar H_2 absorbers from Ledoux et al. (2003) for which Srianand et al. (2005) have performed a systematic search for the presence of C I. We also included a sample of C I-selected quasar absorbers with measurements of C I and H_2 (Noterdaeme et al. 2018), and the same sample of ES-DLAs described above. For all the GRB-host absorbers, C I is only detected in systems with molecular fractions above $f_{H_2} > 10^{-3}$. While C I is also only observed in GRB-host absorbers with relative large metallicities ([X/H] ≳ −1.5), a similar condition appears to be required for the presence of H_2. The detection of C I in GRB H_2 absorbers is, therefore, not specifically related to the metallicity of the systems. From the same samples, we also find that the total column density of C I appears to be linearly correlated with the molecular-hydrogen

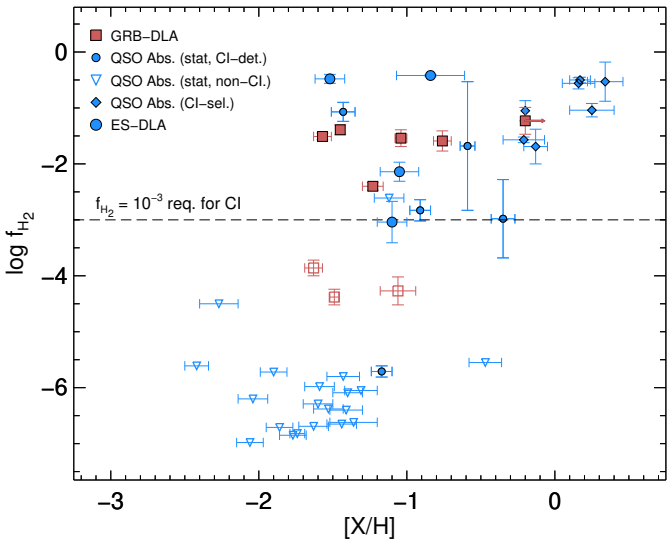

Fig. 12. Molecular-hydrogen fraction as a function of metallicity for the H_2-bearing GRB absorbers (red). Filled squares denote GRBs where C I is also detected, whereas empty squares represent GRBs with H_2 but non-detections of C I. The statistical sample of quasar absorbers from Ledoux et al. (2003) are shown as the small blue symbols where circles denote absorbers with H_2 detections and triangles show the upper limits on the molecular-hydrogen fractions of the absorbers with non-detections of H_2. Filled blue symbols denote quasar absorbers where Srianand et al. (2005) detected C I in absorption, whereas empty blue symbols represent quasar absorbers with non-detections of C I. For comparison, the C I-selected quasar absorbers with measurements of C I, H_2 (Noterdaeme et al. 2018) and metallicities from the literature, are shown as the filled blue diamond symbols. The large blue dots represent the same ES-DLAs as shown in Fig. 10.

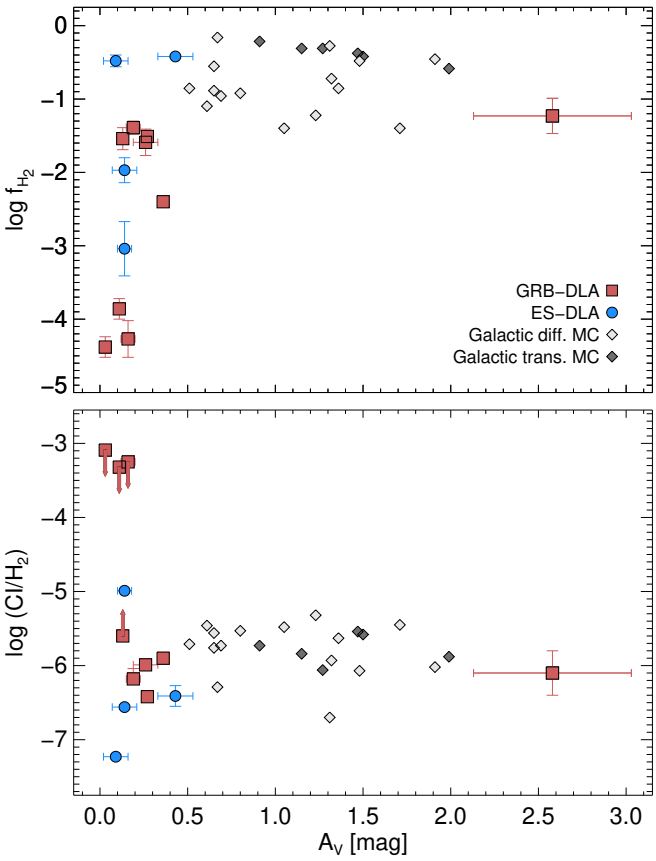

Fig. 13. Molecular-hydrogen fraction and C I/H_2 as a function of visual extinction, A_V. Red squares represent the GRBs from this work. The large blue dots represent the same ES-DLAs as shown in Fig. 10. Diamond symbols show Galactic sightlines where dark gray-filled (resp. light gray-filled) symbols denote diffuse (resp. translucent) molecular clouds (Burgh et al. 2010).

fraction (see also Noterdaeme et al. 2018). This could indicate that a certain fraction of molecular gas is required to efficiently form and subsequently shield C I. The molecular-hydrogen fraction is therefore likely the primary driver for the presence of C I in H_2-bearing GRB-host absorbers.

4.4. Connection between dust and molecular gas

The amount of C I has been observed to be correlated with the visual extinction, A_V, in the line of sight to quasar and GRB absorbers (Ledoux et al. 2015; Ma et al. 2018; Heintz et al. 2019a), suggesting a common origin for the main extinction-derived dust component and C I (see also Heintz et al. 2019b). In Fig. 13, we compare the measured A_V of the H_2-bearing GRB-host absorbers to the relative molecular gas abundance ratios, in terms of f_{H_2} and N(C I/H_2). For comparison, the ES-DLAs with positive H_2 detections compiled from the literature are also shown, in addition to Galactic molecular-rich sightlines from the sample of Burgh et al. (2010), divided into populations of translucent or diffuse molecular clouds.

For the GRB-host absorbers, we note that there is tentative evidence for a relation between the molecular-hydrogen fraction, f_{H_2}, and A_V. As an example, GRB 080607 shows the largest dust content and highest molecular-hydrogen fraction in our sample. Computing the Kendall-rank correlation coefficient τ for f_{H_2} vs A_V yields $\tau = 0.5$. The significance of the correlation is therefore only 1.7σ. We also note that there is tentative evidence for a relation between the relative C I/H_2 abundance ratio and A_V, with $\tau = 0.6$ at 1.5σ confidence, including only the GRB-host absorber with C I detected in absorption. This analysis is limited by the small number of systems in our sample and the small range of (small) A_V values, however, such that the derived correlations only hint at a possible connection between the amount of dust and the relative molecular gas abundance ratios. We note though, that the relatively steep rise and subsequent flattening of the relative C I-to-H_2 abundance ratio at $A_V = 0.5$ mag is consistent with the expected transition regime where C II is converted to C I (Bolatto et al. 2013).

4.5. Kinematics

Direct localization of the absorbing molecular gas and the explosion sites in the GRB host galaxies would provide valuable information of the immediate physical conditions of the absorbing medium. At high redshifts, however, it is challenging to obtain deep resolved images, which is required to map the varying galaxy properties accurately (but see e.g., McGuire et al. 2016; Lyman et al. 2017). As an alternative, we can examine the relative velocity of the C I and H_2 absorption line profiles tracing the molecular gas and compare them to the peak optical depth of the other typically observed line complexes originating from distinct gas-phase components of the ISM. Here we assume that each velocity component represents a discrete cloud in the host galaxy, located in the line of sight to the GRB. Specifically, we compare the H_2 and C I absorption components to the line profiles from singly-ionized fine-structure transitions (typically Fe II*), and low-ionization (typically Fe II, Cr II, Mn II, or Si II)

and high-ionization (N V) metal lines. The relative velocity of fine-structure lines in GRB afterglow spectra carry information on the absorbing gas UV-pumped by the GRB (typically at distances 0.5–2 kpc from the explosion site, e.g., Vreeswijk et al. 2007, 2011; D'Elia et al. 2011). The bulk of the metals in the neutral gas-phase of the GRB-host absorption systems is traced by the low-ionization metal lines, whereas the high-ionization lines (specifically N V) have been argued to trace gas in the vicinity of the GRB (within 10 pc; Prochaska et al. 2008; Heintz et al. 2018).

We find that in the majority of bursts, the relative velocity of the observed H_2 and C I line profiles are kinematically "cold", being offset by $\delta v \lesssim 20\,\mathrm{km\,s^{-1}}$ from the strongest low- and high-ionization and fine-structure line components. Due to the medium resolution of the data, these low offsets should be treated as being consistent with zero. By association, we argue that the different gas-phase components probed by the various lines suggest that they originate from the same approximate region as the bulk of the neutral gas. The fact that N V is coincident with the bulk of the neutral absorbing gas in these GRB-host absorption systems is, however, likely due to their high N(H I), which might confine the gas to the central regions of the host galaxy (Heintz et al. 2018) and is likely related to the GRB event itself.

The two exceptions are GRBs 121024A and 150403A. Friis et al. (2015) showed that for GRB 121024A, the redshift of the Lyman-Werner lines of molecular hydrogen is coincident with the strongest low-ionization metal components, which we also confirm from the C I line profiles. However, the absorption profiles reveal an additional metal line complex at $\delta v \approx -400\,\mathrm{km\,s^{-1}}$ which in turn is coincident with the fine-structure line transitions from Fe II* and Ni II*. The absorbing molecular gas in the GRB host is therefore likely at even greater distances from the explosion site than the gas photoexcited by the GRB (which was found to be at a distance of ≈600 pc; Friis et al. 2015). For GRB 150403A, we find that the peak optical depth of C I is coincident with the strongest components from the low-ionization and fine-structure lines, but offset by $\delta v \approx -30\,\mathrm{km\,s^{-1}}$ from N V (see also Heintz et al. 2018).

5. Discussion

We have now established that GRB-host absorbers can be used to probe the diffuse molecular gas-phase in their high-z star-forming galaxies. Additionally, we were able to quantify the defining characteristics of the subset of H_2-rich absorbers showing the presence of C I and H_2^*. This section is aimed at further understanding the physical properties of the molecular gas in high-z GRB absorbers and explore the possible consequence of a severe dust bias in the detection of H_2-bearing GRB absorbers.

5.1. Excitation temperature

One of the key physical properties of the cold neutral medium (CNM) is the temperature, which is typically found to be in the range 30–100 K for diffuse molecular clouds (Snow & McCall 2006). For the H_2-bearing GRB-host absorbers we can infer the excitation temperature of the molecular gas from

$$\frac{N(\mathrm{H_2},\,j)}{N(\mathrm{H_2},\,i)} = \frac{g(\mathrm{H_2},\,j)}{g(\mathrm{H_2},\,i)} \exp^{-E_{ij}/kT_{ij}}, \quad (2)$$

where g is the spin statistical weight $g(j) = 2j + 1$, E_{ij} is the energy difference between levels i and j, and T_{ij} is the excitation

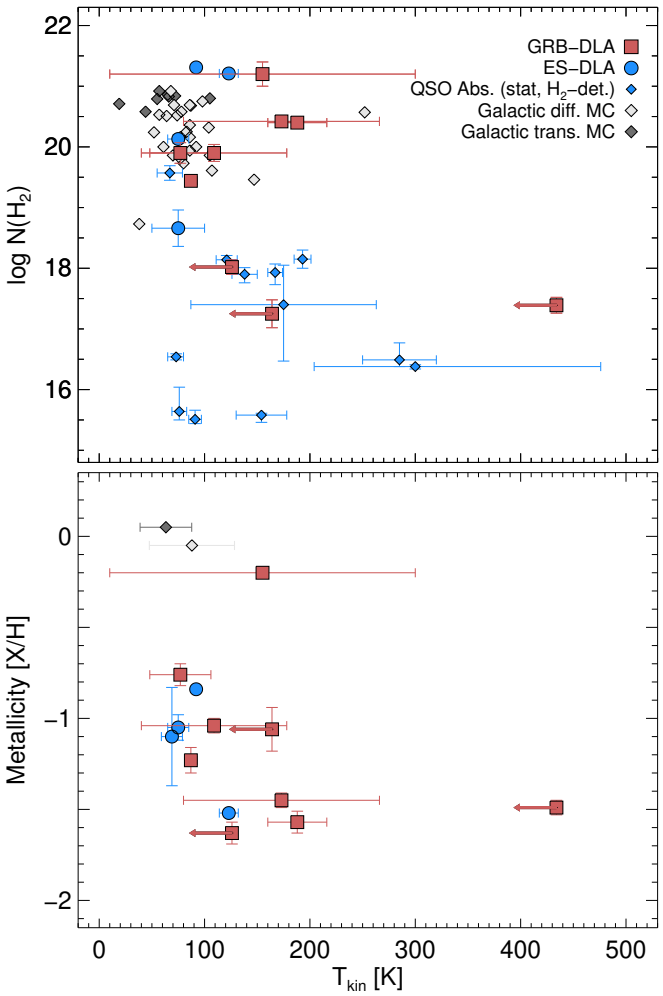

Fig. 14. Measurements of the kinetic temperature from the H_2 rotational excited states as a function of total H_2 column density (*top*) and metallicity (*bottom*). Red squares represent the GRBs from this work, where the arrows mark the upper limits on $T_{\rm kin}$ derived from T_{12} (see text). The small blue diamond symbols denote quasar DLAs from the sample studied by Srianand et al. (2005), where large blue dots represent the same ES-DLAs shown in Fig. 10. The gray-shaded diamond symbols in the top panel again show selected sightlines through diffuse and translucent molecular clouds in the Milky Way (from Burgh et al. 2010). In the bottom panel, only the strongest DLAs with $N(\mathrm{H\,I}) > 10^{21.7}\,\mathrm{cm^{-2}}$ are shown. The gray-shaded diamond symbols here represent the mean $T_{\rm kin}$ for Galactic diffuse and translucent molecular clouds (with error bars denoting the standard deviation), arbitrarily placed at solar metallicities.

temperature. The temperature determined from the lowest two rotational levels ($J = 0$ and $J = 1$), T_{01}, is found to be a good representation of the overall kinetic temperature of the thermalized molecular gas (Roy et al. 2006), whereas higher rotational levels typically indicate larger excitation temperatures due to molecule formation and/or UV pumping.

For the GRBs 120815A, 121024A, 150403A, 181020A, and 190114A, where the H_2 column densities in the two lowest rotational states are well constrained, we are able to robustly measure $T_{01} = T_{\rm kin}$. For the other systems with H_2 detections (i.e., GRBs 120327A, 120909A, and 141109A), the $J = 0$ state is not well constrained by the fit. For these bursts, the derived T_{01} becomes negative, which could suggest that the assumption of equilibrium may not be correct in these cases. To overcome this, we instead compute the excitation temperature from the first

two excited states, T_{12}, but only consider those as upper limits for the kinetic temperature since it is typically found that $T_{12} > T_{01}$ (e.g., Srianand et al. 2005). For GRB 080607, Prochaska et al. (2009) estimated an excitation temperature in the range $T_{ex} = 10-300$ K. The inferred molecular gas temperatures and upper limits are shown in Fig. 14 as a function of $N(H_2)$. Here, we also compare the GRB H_2 absorbers to the H_2-bearing quasar absorbers examined by Srianand et al. (2005), the sample of H_2-bearing ES-DLAs and Galactic molecular clouds (Burgh et al. 2010). In general, the H_2-bearing GRB absorbers contain the largest H_2 column densities observed at high redshift, comparable to quasar ES-DLAs and Galactic molecular clouds. We infer kinetic temperatures in the range $T_{kin} \approx 100-300$ K, consistent with the majority of H_2-bearing quasar absorbers (Srianand et al. 2005; Balashev et al. 2017). We note that there appears to be tentative evidence for the highest metallicity GRB-host and ES-DLA systems to show lower excitation temperatures at a given H_2 column density (see Fig. 14), but only at low significance due to the limited data at hand. Computing the Spearman ρ and Kendall-rank τ correlation coefficients for T_{ex} vs. [X/H] yield $\rho = -0.67$ and $\tau = -0.49$, such that the correlation significance is 2.01σ (considering only the measurements and excluding limits).

We also examine the higher rotational transitions of H_2 in the afterglow spectra of GRBs 181020A and 190114A, which might provide clues on the more external layers of the cloud and the incident UV flux. The column densities of the $J \geq 4$ transitions are not well-constrained in either case, so instead of fitting the individual line transitions we produce a synthetic spectrum, including all J transitions up to $J = 7$, to match to the data. For both GRBs, we fix the redshift and total H_2 column density to the already-determined values and only increase the excitation temperature. We assume a conservative b-parameter of $b = 10\,\mathrm{km\,s^{-1}}$ in both models, since the high-J levels are typically found to show broader features than the low-J transitions (see, e.g., Noterdaeme et al. 2007). For GRB 181020A, the spectrum does not show any clear indication of features arising from the $J \geq 4$ transitions, suggesting that none of the high-J transitions are significantly populated. Based on our model, we estimate that a maximum high-J excitation temperature of $T_{ex} \sim 300$ K is consistent with the observed spectrum. For GRB 190114A, we find that the spectrum is consistent with high-J features arising from a warmer medium, constrained to $T_{ex} \sim 500$ K. This would indicate that the intensity of the ambient UV field in the host of GRB 190114A is higher compared to the host of GRB 181020A. It is in principle possible to indirectly measure the ambient UV flux from the fine-structure transition of C II* λ1335 (Wolfe et al. 2003). However, in both the afterglow spectra of GRBs 181020A and 190114A this feature is either saturated or blended with C II λ1334.

5.2. Implications of a dust bias for H_2 detection

With the increased number of known H_2-bearing GRB absorbers, it is clear that the first apparent bias against this subpopulation (Tumlinson et al. 2007; Whalen et al. 2008; Ledoux et al. 2009) is partly alleviated. This is largely owing to the more sensitive, higher-resolution X-shooter spectrograph, with which a large statistical sample of GRBs has been obtained (Selsing et al. 2019). Expanding the discussion from Krühler et al. (2013), we now wish to quantify to what extent the XS-GRB sample is biased against the most metal- and dust-rich H_2-bearing GRB-host absorption systems. Specifically whether a significant dust bias exists decreasing the H_2 detection probability in these systems.

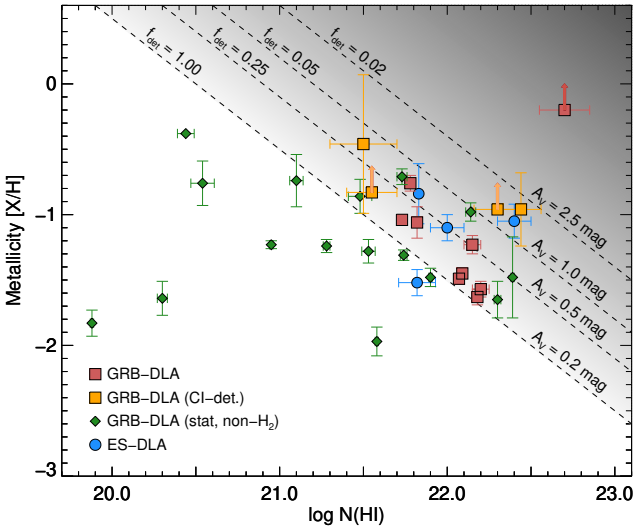

Fig. 15. Gas-phase metallicity as a function of H I column density. Filled red squares represent the GRBs from this work with positive H_2 detections, orange squares denote C I-bearing GRBs (where H_2 could not be constrained) from this work or Heintz et al. (2019a) and the green diamond symbols show the statistical GRB-DLA sample from Bolmer et al. (2019) without H_2 detections. For comparison, the large blue dots show the same ES-DLAs as shown in Fig. 10. The gray-shaded region and overplotted dashed lines show the expected increase in A_V for a given dust-to-metals ratio, in addition to the estimated detection probability f_{det} of dusty H_2-bearing GRB absorbers (see Sect. 5.2 for further details).

To do so, we compare the A_V distribution of the statistical sample of XS-GRBs, from which Bolmer et al. (2019) searched for H_2, to an unbiased sample of GRB afterglows (Covino et al. 2013). We normalize the two distributions to the number of bursts with $A_V < 0.2$ mag (which we expect the XS-GRB sample to at least be complete to) and compute the fraction of H_2-bearing GRBs to the number of bursts in the unbiased sample in bins of $A_V = 0.2-0.5$, 0.5–1.0, and 1.0–2.5 mag. We find that already at $A_V = 0.2-0.5$ mag, the detection probability of the bursts in the XS-GRB sample only constitutes ~25% of the underlying distribution. At $A_V = 0.5-1.0$ mag we estimate the fraction of uncovered GRB H_2 absorbers to be ~5%, based only on the detection of C I in GRB 120119A which was not part of the statistical H_2 sample so this fraction effectively only serves as an upper limit. Similarly for the $A_V = 1.0-2.5$ mag range, we estimate the detection probability to be 2%, based on the single detection of H_2 in GRB 080607 in the unbiased sample of ~50 bursts by Covino et al. (2013). Again, the detection probability is likely lower since none of the H_2-bearing XS-GRBs show A_V in this range. This is illustrated in Fig. 15, where we show the metallicity as a function of H I column density of the GRB absorbers and compare to the expected dust extinction for a given dust-to-metals ratio (Zafar & Watson 2013). These estimates do not take into account the increased difficulty of detecting H_2 in faint bursts (either intrinsically or due to overall stronger dust absorption) and also do not include the possibility of steep extinction curves. For example, GRB 140506A (Fynbo et al. 2014; Heintz et al. 2017) would be practically invisible at optical wavelengths if it were located at $z \gtrsim 2$. The dust bias in the observed XS-GRB sample might therefore be even more severe than the simple estimates provided here.

We wish to emphasize though, that if a spectrum of a burst similar to GRB 180325A (with strong C I absorption and $A_V \sim 1.5$ mag) was obtained with higher S/N spectroscopy, the H_2 features might have been revealed as well. Conversely, this

further demonstrates the versatility of using C I as an alternative tracer of molecular gas, even in very dust-reddened sightlines. We conclude that the large majority of dusty ($A_V > 0.2$ mag) H_2-bearing GRBs are missed due to a significant dust bias. This confirms the proposal by Ledoux et al. (2009), that GRB-host absorber samples are likely to be biased against dusty and metal-rich sightlines. Only in the cases of rare, extremely luminous afterglows (such as GRB 080607; Prochaska et al. 2009; Perley et al. 2011) is it possible to detect H_2 in the most dust-obscured GRB sightlines.

6. Conclusions

We have presented optical to NIR VLT/X-shooter spectroscopy of the afterglows of GRBs 181020A and 190114A at $z = 2.938$ and $z = 3.376$, respectively. Both sightlines are characterized by strong DLAs and substantial amounts of molecular hydrogen with $\log N(\mathrm{H\,I}, H_2) = 22.20 \pm 0.05$, 20.40 ± 0.04 (GRB 181020A) and $\log N(\mathrm{H\,I}, H_2) = 22.15 \pm 0.05$, 19.44 ± 0.04 (GRB 190114A). Both GRB-host absorption systems show relatively high molecular fractions of $f_{H_2} = 0.4-3\%$, characteristic of Galactic diffuse molecular gas and consistent with the majority of H_2-bearing quasar absorbers at high-z. These two cases represent only the eighth and ninth unambiguous detection of H_2 in GRB-host absorption systems. We measure gas-phase metallicities of $[\mathrm{Zn/H}] = -1.57 \pm 0.06$ and -1.23 ± 0.07, relative depletion abundances of $[\mathrm{Zn/Fe}] = 0.67 \pm 0.03$ and 1.06 ± 0.08, and visual extinctions of $A_V = 0.27 \pm 0.02$ mag and 0.36 ± 0.02 mag, for GRB 181020A and GRB 190114A, respectively. While the metallicities of the two systems are relatively low and comparable to typical GRB-host absorbers, their metal column densities, $\log N(\mathrm{H\,I}) + [\mathrm{Zn/H}]$, are among the highest in the general GRB-host absorber population. They are also both well above the apparent GRB H_2 detection threshold of $\log N(\mathrm{H\,I}) + [\mathrm{Zn/H}] > 20.5$ (Bolmer et al. 2019).

In addition to molecular hydrogen, we also detect absorption features from neutral atomic carbon and vibrationally-excited H_2 in both afterglow spectra of GRBs 181020A and 190114A. To complement the analysis of these alternative molecular gas tracers, and to explore the conditions for these rarer absorption features to arise, we systematically searched all the H_2-bearing GRB absorbers from Bolmer et al. (2019) for the presence of C I or H_2^* and measured or provided limits on the respective column densities. We found that C I and H_2^* are efficient tracers of H_2-rich GRB-host absorbers, but also that H_2 does not guarantee the presence of either. First, we explored the conditions required to detect C I in the H_2-bearing GRB absorbers and we found that an apparent threshold of the overall molecular-hydrogen fraction of $f_{H_2} > 10^{-3}$ is essential. The total C I column density is also found to be linearly connected with f_{H_2}. The defining characteristic for the presence of H_2^* is less clear, likely because it depends on several parameters such as the H_2 abundance, GRB luminosity and distance to the absorbing molecular gas. This somewhat limits the applications of C I and H_2^* as overall efficient molecular gas tracers. On the other hand, identifying absorption features from C I or H_2^* provides indirect evidence of large H_2 abundances, even in the absence of the Lyman-Werner H_2 features (e.g., due to low redshifts, large dust content or low spectral resolution). We also compared the kinematics of the absorption lines from the molecular gas tracers C I and H_2 to the low- and high-ionization and fine-structure absorption features typically observed in GRB-host absorbers. We found that C I and H_2 are in most cases kinematically "cold", thus likely confined to the same proximate region as the bulk of the metals producing the strongest low- and high-ionization absorption features.

Based on the now nine positive detections of H_2 in GRB-host absorbers, we examined the typical excitation temperatures of the molecular gas, constrained from the two lowest rotational levels of H_2 ($J = 0, 1$). For the systems in our sample we inferred temperatures in the range $T_{ex} = 100-300$ K. A more careful analysis of the high-J H_2 transitions in GRBs 181020A and 190114A revealed tentative evidence of a slightly warmer component with up to $T_{ex} = 300$ and 500 K, respectively. Finally, we determined the probability of detecting H_2 in the XS-GRB afterglow sample (Selsing et al. 2019) as a function of A_V. Even in moderately extinguished sightlines with $A_V \gtrsim 0.2$ mag, the number density of GRB H_2 absorbers drops to ~25% compared to an unbiased sample of GRB afterglows. This suggests that while the XS-GRB afterglow survey has been successful in recovering a significant number of H_2-bearing GRB absorbers (Bolmer et al. 2019), the most dust-obscured systems are still missed due to a non-negligible dust bias.

In summary, GRB-host absorbers provide detailed information about the characteristics and physical properties of the diffuse molecular gas-phase in the ISM of star-forming galaxies during the peak of cosmic star-formation. While the absorption features of the molecular gas tracers are typically only detected at UV/optical wavelengths, there are promising prospects of detecting them at sub-mm wavelengths in ALMA spectroscopy as well (de Ugarte Postigo et al. 2018). Connecting the properties inferred from absorption-line analyses to the CO line emission at sub-mm wavelengths would also provide unparalleled insight into the conditions and physical processes fuelling star-formation at high redshift. So far, only a small number of high-z GRB host galaxies have been detected in emission from CO (Michałowski et al. 2018; Arabsalmani et al. 2018), though without any constraints on the molecular gas properties from absorption. Targeting the CO emission lines of this sample of H_2-bearing GRB-host galaxy absorbers would provide a natural unification of the two approaches. In the near future, identification of the vibrational and ro-vibrational H_2 emission lines will also be possible with the *James Webb* Space Telescope (Kalirai 2018) at $z \gtrsim 2$ where H_2 can be detected in absorption (Guillard et al. 2015), which so far has only been detected in a single, $z \sim 0.1$ GRB host (Wiersema et al. 2018). This combined analysis of molecular gas in line-of-sight GRB afterglow spectra and integrated host galaxy spectra will also greatly benefit the typically more extensive emission-selected CO galaxy surveys, and significantly improve our understanding of the connection between cold and molecular gas observed in absorption and emission.

Acknowledgements. We would like to thank the referee for a clear, concise, and timely report. KEH and PJ acknowledge support by a Project Grant (162948–051) from The Icelandic Research Fund. PN and JKK acknowledge support from the French Agence Nationale de la Recherche under contract ANR-17-CE31-0011-01 (Projet "HIH2", PI Noterdaeme) and are grateful to the European Southern Observatory for hospitality and support during a visit to the ESO headquarters in Chile. The Cosmic Dawn Center is funded by the DNRF. AdUP, CCT, DAK and LI acknowledge support from the Spanish research project AYA2017-89384-P, and from the State Agency for Research of the Spanish MCIU through the "Center of Excellence Severo Ochoa" award for the Insituto de Astrofísica de Andalucía (SEV-2017-0709). AdUP and CCT acknowledge support from Ramón y Cajal fellowships (RyC-2012-09975 and RyC-2012-09984). LI acknowledges support from a Juan de la Cierva Incorporación fellowship (IJCI-2016-30940).

References

Arabsalmani, M., Le Floc'h, E., Dannerbauer, H., et al. 2018, MNRAS, 476, 2332

Asplund, M., Grevesse, N., Sauval, A. J., & Scott, P. 2009, ARA&A, 47, 481
Balashev, S. A., & Noterdaeme, P. 2018, MNRAS, 478, L7
Balashev, S. A., Klimenko, V. V., Ivanchik, A. V., et al. 2014, MNRAS, 440, 225
Balashev, S. A., Noterdaeme, P., Klimenko, V. V., et al. 2015, A&A, 575, L8
Balashev, S. A., Noterdaeme, P., Rahmani, H., et al. 2017, MNRAS, 470, 2890
Barthelmy, S. D., Barbier, L. M., Cummings, J. R., et al. 2005, Space Sci. Rev., 120, 143
Bolatto, A. D., Wolfire, M., & Leroy, A. K. 2013, ARA&A, 51, 207
Bolmer, J. 2019, Dissertation, München Technische Universität München
Bolmer, J., Greiner, J., Krühler, T., et al. 2018, A&A, 609, A62
Bolmer, J., Ledoux, C., Wiseman, P., et al. 2019, A&A, 623, A43
Burgh, E. B., France, K., & Jenkins, E. B. 2010, ApJ, 708, 334
Carilli, C. L., & Walter, F. 2013, ARA&A, 51, 105
Chen, H.-W., Perley, D. A., Pollack, L. K., et al. 2009, ApJ, 691, 152
Covino, S., Melandri, A., Salvaterra, R., et al. 2013, MNRAS, 432, 1231
De Cia, A., Ledoux, C., Mattsson, L., et al. 2016, A&A, 596, A97
de Ugarte Postigo, A., Thöne, C. C., Bolmer, J., et al. 2018, A&A, 620, A119
de Ugarte Postigo, A., Tanvir, N. R., Xu, D., & Fynbo, J. 2019, GRB Coordinates Network, Circular Service, No. 23680, 23680
D'Elia, V., Campana, S., Covino, S., et al. 2011, MNRAS, 418, 680
D'Elia, V., Fynbo, J. P. U., Goldoni, P., et al. 2014, A&A, 564, A38
Draine, B. T. 2000, ApJ, 532, 273
Draine, B. T., & Hao, L. 2002, ApJ, 569, 780
Friis, M., De Cia, A., Krühler, T., et al. 2015, MNRAS, 451, 167
Fynbo, J. P. U., de Ugarte Postigo, A., D'Elia, V., et al. 2018, GRB Coordinates Network, Circular Service, No. 23356, 23356
Fynbo, J. P. U., Starling, R. L. C., Ledoux, C., et al. 2006, A&A, 451, L47
Fynbo, J. P. U., Jakobsson, P., Prochaska, J. X., et al. 2009, ApJS, 185, 526
Fynbo, J. P. U., Krühler, T., Leighly, K., et al. 2014, A&A, 572, A12
Galama, T. J., & Wijers, R. A. M. J. 2001, ApJ, 549, L209
Ge, J., & Bechtold, J. 1999, in Highly Redshifted Radio Lines, eds. C. L. Carilli, S. J. E. Radford, K. M. Menten, & G. I. Langston, ASP Conf. Ser., 156, 121
Gehrels, N., Chincarini, G., Giommi, P., et al. 2004, ApJ, 611, 1005
Gordon, K. D., Clayton, G. C., Misselt, K. A., Landolt, A. U., & Wolff, M. J. 2003, ApJ, 594, 279
Greiner, J., Fox, D. B., Schady, P., et al. 2015, ApJ, 809, 76
Guillard, P., Boulanger, F., Lehnert, M. D., Appleton, P. N., & Pineau des Forêts, G. 2015, SF2A-2015: Proceedings of the Annual Meeting of the French Society of Astronomy and Astrophysics, 81
Guimarães, R., Noterdaeme, P., Petitjean, P., et al. 2012, AJ, 143, 147
Hatsukade, B., Ohta, K., Endo, A., et al. 2014, Nature, 510, 247
Heintz, K. E., Fynbo, J. P. U., Jakobsson, P., et al. 2017, A&A, 601, A83
Heintz, K. E., Watson, D., Jakobsson, P., et al. 2018, MNRAS, 479, 3456
Heintz, K. E., Ledoux, C., Fynbo, J. P. U., et al. 2019a, A&A, 621, A20
Heintz, K. E., Zafar, T., De Cia, A., et al. 2019b, MNRAS, 486, 2063
Jakobsson, P., Hjorth, J., Fynbo, J. P. U., et al. 2004, A&A, 427, 785
Jakobsson, P., Fynbo, J. P. U., Ledoux, C., et al. 2006, A&A, 460, L13
Japelj, J., Covino, S., Gomboc, A., et al. 2015, A&A, 579, A74
Jorgenson, R. A., Murphy, M. T., Thompson, R., & Carswell, R. F. 2014, MNRAS, 443, 2783
Kalirai, J. 2018, Contemp. Phys., 59, 251
Kennicutt, R. C., & Evans, N. J. 2012, ARA&A, 50, 531
Krogager, J. K. 2018, ArXiv e-prints [arXiv:1803.01187]
Krogager, J.-K., Fynbo, J. P. U., Noterdaeme, P., et al. 2016, MNRAS, 455, 2698
Krühler, T., Ledoux, C., Fynbo, J. P. U., et al. 2013, A&A, 557, A18
Laporte, S. J., Kennea, J. A., Klingler, N. J., et al. 2019, GRB Coordinates Network, Circular Service, No. 23677, 23677
Ledoux, C., Petitjean, P., & Srianand, R. 2003, MNRAS, 346, 209
Ledoux, C., Vreeswijk, P. M., Smette, A., et al. 2009, A&A, 506, 661
Ledoux, C., Noterdaeme, P., Petitjean, P., & Srianand, R. 2015, A&A, 580, A8
Lien, A., Sakamoto, T., Barthelmy, S. D., et al. 2016, ApJ, 829, 7
Lodders, K., Palme, H., & Gail, H. P. 2009, Landolt Bernstein, 4B, 712
Lyman, J. D., Levan, A. J., Tanvir, N. R., et al. 2017, MNRAS, 467, 1795
Ma, J., Ge, J., Prochaska, J. X., et al. 2018, MNRAS, 474, 4870
McGuire, J. T. W., Tanvir, N. R., Levan, A. J., et al. 2016, ApJ, 825, 135
McKee, C. F., & Ostriker, E. C. 2007, ARA&A, 45, 565
Mészáros, P. 2006, Rep. Prog. Phys., 69, 2259
Michałowski, M. J., Castro Cerón, J. M., Wardlow, J. L., et al. 2016, A&A, 595, A72
Michałowski, M. J., Karska, A., Rizzo, J. R., et al. 2018, A&A, 617, A143
Modigliani, A., Goldoni, P., Royer, F., et al. 2010, in Observatory Operations: Strategies, Processes, and Systems III, Proc. SPIE, 7737, 773728
Moss, M. J., D'Ai, A., D'Elia, V., et al. 2018, GRB Coordinates Network, Circular Service, No. 23349, 23349
Noterdaeme, P., Petitjean, P., Srianand, R., Ledoux, C., & Le Petit, F. 2007, A&A, 469, 425
Noterdaeme, P., Ledoux, C., Petitjean, P., & Srianand, R. 2008, A&A, 481, 327
Noterdaeme, P., Petitjean, P., Pâris, I., et al. 2014, A&A, 566, A24
Noterdaeme, P., Srianand, R., Rahmani, H., et al. 2015, A&A, 577, A24
Noterdaeme, P., Ledoux, C., Zou, S., et al. 2018, A&A, 612, A58
Palmerio, J. T., Vergani, S. D., Salvaterra, R., et al. 2019, A&A, 623, A26
Perley, D. A., Morgan, A. N., Updike, A., et al. 2011, AJ, 141, 36
Perley, D. A., Tanvir, N. R., Hjorth, J., et al. 2016, ApJ, 817, 8
Planck Collaboration XIII. 2016, A&A, 594, A13
Prochaska, J. X. 2006, ApJ, 650, 272
Prochaska, J. X., Chen, H.-W., Dessauges-Zavadsky, M., & Bloom, J. S. 2007, ApJ, 666, 267
Prochaska, J. X., Dessauges-Zavadsky, M., Ramirez-Ruiz, E., & Chen, H.-W. 2008, ApJ, 685, 344
Prochaska, J. X., Sheffer, Y., Perley, D. A., et al. 2009, ApJ, 691, L27
Ranjan, A., Noterdaeme, P., Krogager, J.-K., et al. 2018, A&A, 618, A184
Roy, N., Chengalur, J. N., & Srianand, R. 2006, MNRAS, 365, L1
Salvaterra, R. 2015, J. High Energy Astrophys., 7, 35
Salvaterra, R., Della Valle, M., Campana, S., et al. 2009, Nature, 461, 1258
Schlafly, E. F., & Finkbeiner, D. P. 2011, ApJ, 737, 103
Schlegel, D. J., Finkbeiner, D. P., & Davis, M. 1998, ApJ, 500, 525
Selsing, J., Malesani, D., Goldoni, P., et al. 2019, A&A, 623, A92
Sheffer, Y., Rogers, M., Federman, S. R., et al. 2008, ApJ, 687, 1075
Sheffer, Y., Prochaska, J. X., Draine, B. T., Perley, D. A., & Bloom, J. S. 2009, ApJ, 701, L63
Snow, T. P., & McCall, B. J. 2006, ARA&A, 44, 367
Solomon, P. M., & Vanden Bout, P. A. 2005, ARA&A, 43, 677
Srianand, R., Petitjean, P., Ledoux, C., Ferland, G., & Shaw, G. 2005, MNRAS, 362, 549
Stanway, E. R., Levan, A. J., Tanvir, N. R., Wiersema, K., & van der Laan, T. P. R. 2015, ApJ, 798, L7
Tanvir, N. R., Fox, D. B., Levan, A. J., et al. 2009, Nature, 461, 1254
Tanvir, N. R., Laskar, T., Levan, A. J., et al. 2018, ApJ, 865, 107
Tanvir, N. R., Fynbo, J. P. U., de Ugarte Postigo, A., et al. 2019, MNRAS, 483, 5380
Tumlinson, J., Prochaska, J. X., Chen, H.-W., Dessauges-Zavadsky, M., & Bloom, J. S. 2007, ApJ, 668, 667
Vernet, J., Dekker, H., D'Odorico, S., et al. 2011, A&A, 536, A105
Vreeswijk, P. M., Ellison, S. L., Ledoux, C., et al. 2004, A&A, 419, 927
Vreeswijk, P. M., Ledoux, C., Smette, A., et al. 2007, A&A, 468, 83
Vreeswijk, P. M., Ledoux, C., Smette, A., et al. 2011, A&A, 532, C3
Watson, D., Fynbo, J. P. U., Ledoux, C., et al. 2006, ApJ, 652, 1011
Whalen, D., Prochaska, J. X., Heger, A., & Tumlinson, J. 2008, ApJ, 682, 1114
Wiseman, P., Schady, P., Bolmer, J., et al. 2017, A&A, 599, A24
Wiersema, K., Togi, A., Watson, D., et al. 2018, MNRAS, 481, 1126
Wolfe, A. M., Turnshek, D. A., Smith, H. E., & Cohen, R. D. 1986, ApJS, 61, 249
Wolfe, A. M., Prochaska, J. X., & Gawiser, E. 2003, ApJ, 593, 215
Wolfe, A. M., Gawiser, E., & Prochaska, J. X. 2005, ARA&A, 43, 861
Woosley, S. E., & Bloom, J. S. 2006, ARA&A, 44, 507
Zafar, T., & Watson, D. 2013, A&A, 560, A26
Zafar, T., Heintz, K. E., Fynbo, J. P. U., et al. 2018a, ApJ, 860, L21
Zafar, T., Watson, D., Møller, P., et al. 2018b, MNRAS, 479, 1542

Appendix A: Gas-phase abundances and dust extinction toward GRBs 181020A and 190114A

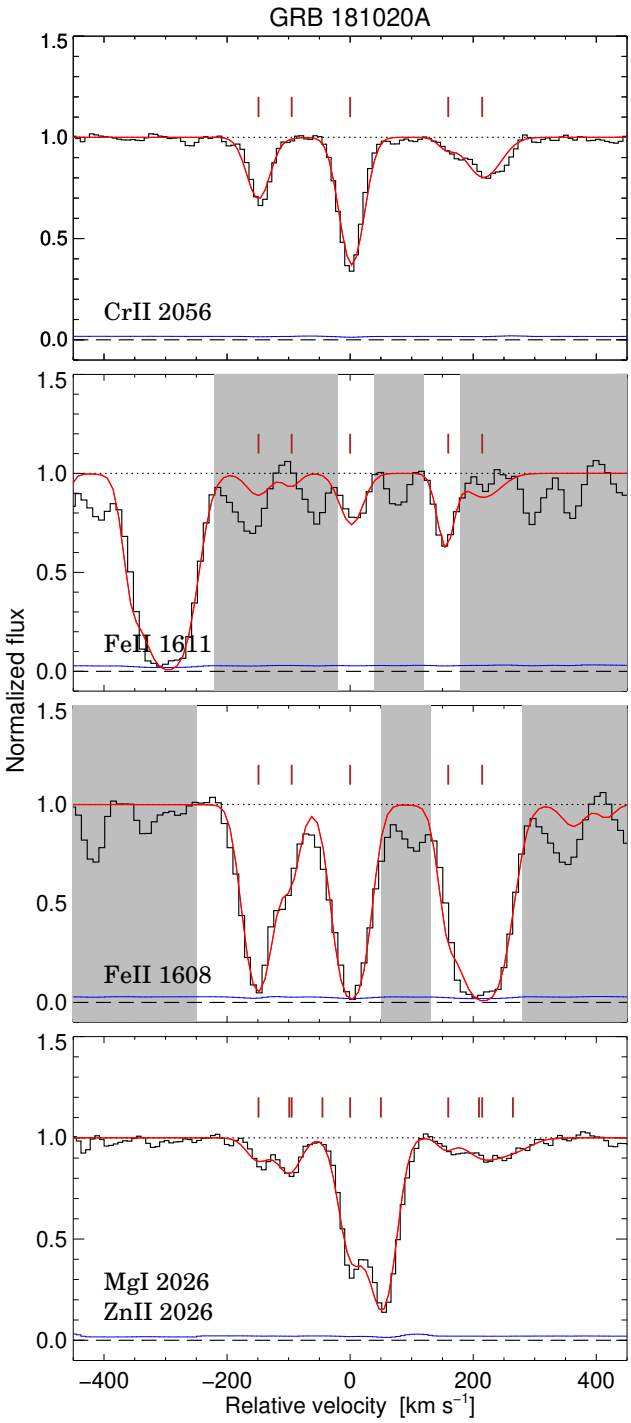

Fig. A.1. Normalized VLT/X-shooter spectrum of GRB 181020A in velocity space, centered on the strongest component at $z = 2.9379$. The solid black line shows the spectrum and the associated error is shown in blue. The best-fit Voigt profiles are indicated by the solid red lines. The identified velocity components are marked above each of the absorption profiles. Gray shaded regions were ignored in the fit. These lines are representative of the typical low-ionization metal lines in GRB 181020A, showing most clearly the overall velocity structure.

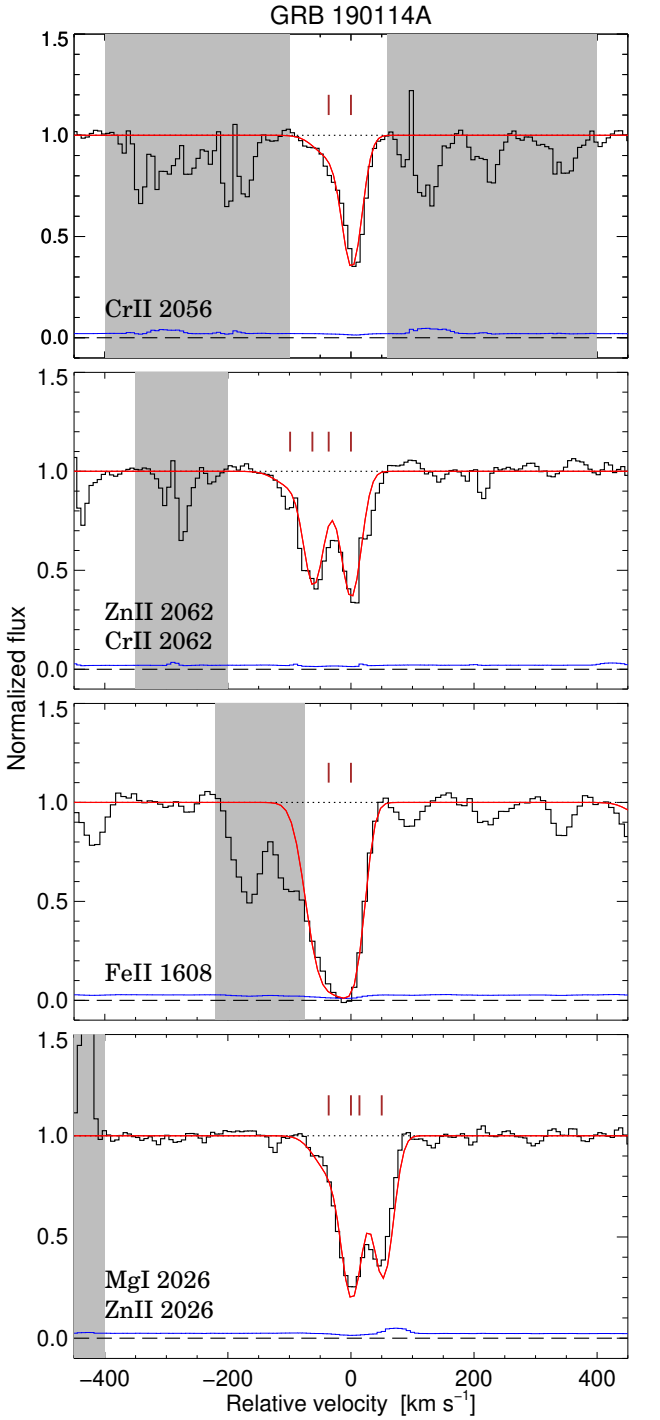

Fig. A.2. Same as Fig. A.1 but for GRB 190114A, centered on $z = 3.3764$.

Here a subset of the low-ionization metal lines observed in the afterglow spectra of GRB 181020A (Fig. A.1) and GRB 190114A (Fig. A.2) is shown. We fit several other transitions, including single-ionized elements not shown in these plots to constrain the velocity components of the absorption line profiles. However, we here only show few selected lines that best represent the overall velocity structure of the line profiles and focus on the elements used to determine the gas-phase abundance and depletion (e.g., Zn II and Fe II). In Figs. A.3 and A.4 we show the best-fit extinction observed toward GRBs 181020A and 190114A, respectively. Both sightlines can be modelled by a smooth, SMC-like extinction curve and are moderately reddened with $A_V = 0.27 \pm 0.02$ mag and $A_V = 0.36 \pm 0.02$ mag, respectively.

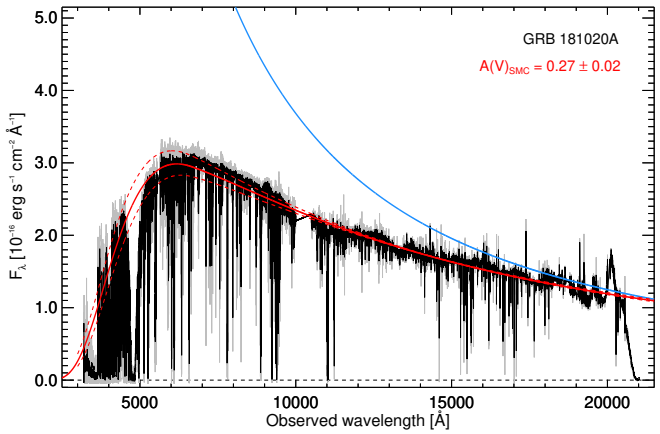

Fig. A.3. Extinction curve fit for GRB 181020A. The raw combined VLT/X-shooter spectrum is shown in gray, overplotted with a binned version to enhance the continuum trace. The best-fit SMC-like extinction with $A_V = 0.27 \pm 0.02$ mag is shown by the solid red line, where the error on the fit is shown by the dashed red lines. The best-fit intrinsic spectral slope is overplotted as the solid blue line.

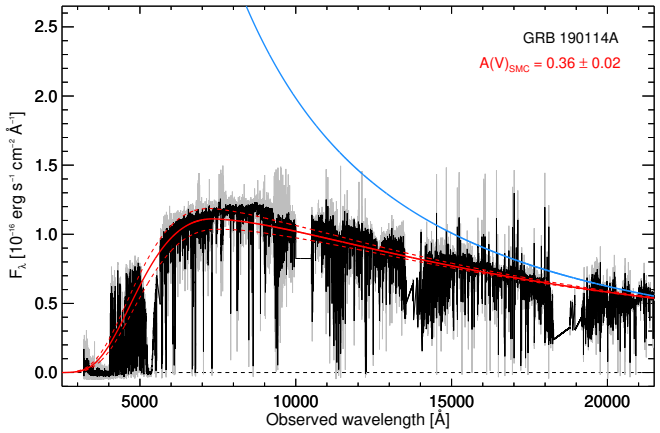

Fig. A.4. Same as Fig. A.3 but for GRB 190114A, with a best-fit SMC-like extinction of $A_V = 0.36 \pm 0.02$ mag.

Appendix B: Individual notes on sample XS-GRBs

Here we provide notes on each individual burst studied in this work. Since we extracted information about the gas-phase abundance and dust extinction from the literature for all our sample bursts, we will mainly focus on the C I line measurements. For all cases, we only detect a single absorption component from C I but we caution that at this spectral resolution, the observed line profiles might actually be comprised of several narrow lines. However, the fits to H_2 for most of the GRBs also indicate that only one component from the molecular-gas phase is present in the spectrum. Any intrinsically narrow absorption components contributing significantly to the observed column densities, would also be present at the location of CO but we do not find any evidence of this.

By modelling a set of synthetic spectra with imposed C I lines with varying b-parameters and N(C I), we estimate that the line profiles are intrinsically saturated for $N(\mathrm{C\,I})_{\mathrm{tot}} \gtrsim 14.5$ (for $b \gtrsim 5\,\mathrm{km\,s^{-1}}$). This is also supported by the typical uncertain broadening parameters associated with the GRBs having the largest C I column densities. For the GRB absorbers where the best-fit value for N(C I) is above this limit (GRBs 120119A, 150403A, and 180325A), we therefore only provide the 2σ lower limit on the C I abundances. For the GRB absorption systems with $N(\mathrm{C\,I}) < 14.5$ (GRBs 120815A, 121024A, 181020A, and 190114A) we report the measured value for each of the C I abundances. These are also all consistent with the linear relation found for the quasar C I absorbers in Sect. 3 (see Fig. 7) between $N(\mathrm{C\,I})_{\mathrm{tot}}$ and the rest-frame C I equivalent widths of the same systems. To further verify the robustness of the column density measurements we produce a set of synthetic spectra with varying b-parameters and perform the same fitting routine as detailed in Sect. 3.4. We are able to recover the input column densities (for non-saturated lines) within the error for all values of $b \gtrsim 2\,\mathrm{km\,s^{-1}}$.

Table B.1. Results of the Voigt-profile fitting for GRB 120119A.

Exc. state (J)	$\log N$(C I) $b = 2.9 \pm 0.5$ (km s^{-1})	$b = 5$ (km s^{-1})
C I	16.85 ± 0.28	15.10 ± 0.51
C I*	16.34 ± 0.66	14.16 ± 0.16
C I**	16.75 ± 0.46	15.13 ± 0.25

Notes. The column densities for $b = 5\,\mathrm{km\,s^{-1}}$ are reported throughout.

B.1. GRB 120119A at z = 1.7288

The spectrum presented here was published by Selsing et al. (2019). The gas-phase abundances listed in Table 1 derived for this GRB are adopted from Wiseman et al. (2017). They found $\log N(\mathrm{H\,I}) = 22.44 \pm 0.12$, $[\mathrm{Zn/H}] = -0.96 \pm 0.28$ and $[\mathrm{Zn/Fe}] = 1.04 \pm 0.35$. Following De Cia et al. (2016) we compute a dust-corrected metallicity, $[\mathrm{M/H}] = [\mathrm{X/H}] - \delta_X$ (where δ_X is inferred from the iron-to-zinc depletion), of $[\mathrm{M/H}] = 0.68 \pm 0.30$. Both Japelj et al. (2015) and Zafar et al. (2018b) have derived the visual extinction of this GRB and found a consistent value of $A_V \sim 1$ mag. We chose to adopt A_V from the latter study (listed in Table 1), since they included a full parametrization of the extinction curve in the fit. It was not possible to examine H_2 in this absorption system due to the low redshift.

To fit the neutral atomic carbon abundances for this GRB we ran two iterations; one where b is left as a free parameter and one where we fix the b-parameter to $5\,\mathrm{km\,s^{-1}}$. The fit was only constrained by the C I $\lambda\lambda$1560,1656 line transitions since the C I $\lambda\lambda$1277,1328 lines were completely blended with telluric absorption features and located in spectral regions with poor S/N. We also masked out one unrelated line in the immediate continuum region of the C I λ1560 transition, although it does not appear to be blended with the line profiles. We obtain a best-fit b-parameter of $b = 2.9 \pm 0.5\,\mathrm{km\,s^{-1}}$. However, given the S/N of the spectrum we are not able to distinguish which fit is preferred for $b \lesssim 5\,\mathrm{km\,s^{-1}}$. The derived column densities for both b-parameters are listed in Table B.1. Since the b-parameter cannot be well-constrained we assume $b = 5\,\mathrm{km\,s^{-1}}$ and derive a 2σ lower limit of $\log N(\mathrm{C\,I})_{\mathrm{tot}} \gtrsim 14.9$ for this GRB. This lower limit takes into account both the uncertain line broadening and the intrinsically saturated line profiles. The best fit Voigt profiles are shown overplotted on the normalized VLT/X-shooter spectrum in Fig. B.1 for $b = 5\,\mathrm{km\,s^{-1}}$.

B.2. GRB 120327A at z = 2.8143

The spectrum presented here was first published by D'Elia et al. (2014), who also reported the presence of H_2 in the spectrum.

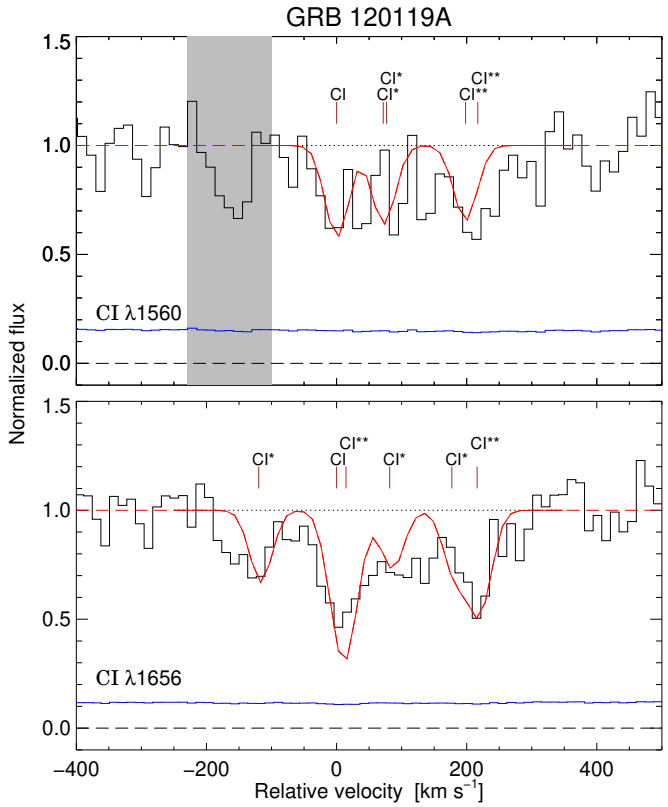

Fig. B.1. Normalized VLT/X-shooter spectrum of GRB 120119A in velocity space, centered on the ground-state C I transitions at $z = 1.72912$. The solid black line shows the spectrum and the associated error is shown in blue. The combined best fit Voigt profiles (with fixed $b = 5\,\mathrm{km\,s^{-1}}$) are indicated by the solid red line, with the dashed red line indicating the continuum. The C I ground-state and excited line transitions are marked above each of the absorption profiles. The gray shaded region was ignored in the fit.

The neutral and molecular gas-phase abundances listed in Table 1 derived for this GRB are adopted from Bolmer et al. (2019). They found $\log N(\mathrm{H\,I}) = 22.07 \pm 0.01$, $\log N(\mathrm{H_2}) = 17.39 \pm 0.13$, $[\mathrm{Zn/H}] = -1.49 \pm 0.03$ and $[\mathrm{Zn/Fe}] = 0.27 \pm 0.07$, resulting in a dust-corrected metallicity of $[\mathrm{M/H}] = -1.34 \pm 0.02$. D'Elia et al. (2014) derived an upper limit on the visual extinction along the line of sight to this GRB of $A_V < 0.03$ mag. We find no evidence for C I in this absorption system (see also Heintz et al. 2019a), and derive a 2σ upper limit of $\log N(\mathrm{C\,I})_{\mathrm{tot}} < 14.3$ assuming $b = 2\,\mathrm{km\,s^{-1}}$.

B.3. GRB 120815A at z = 2.3582

The spectrum presented here was first published by Krühler et al. (2013), who also reported the presence of H_2 and C I in the spectrum. The neutral and molecular gas-phase abundances listed in Table 1 derived for this GRB are adopted from Bolmer et al. (2019). They found $\log N(\mathrm{H\,I}) = 22.09 \pm 0.01$, $\log N(\mathrm{H_2}) = 20.42 \pm 0.08$, $[\mathrm{Zn/H}] = -1.45 \pm 0.03$ and $[\mathrm{Zn/Fe}] = 1.01 \pm 0.05$, resulting in a dust-corrected metallicity of $[\mathrm{M/H}] = -1.23 \pm 0.03$. We adopt the visual extinction derived by Zafar et al. (2018b) of $A_V = 0.19 \pm 0.04$ mag.

To fit the neutral atomic carbon abundances for this GRB we ran the same two iterations as for GRB 120119A. Since we only detect a single absorption component from the C I λ1328 line complex, we fixed this in the fit to the C I $\lambda\lambda$1328,1560,1656 line transitions. The C I λ1277 line was only used to constrain the upper limit on the column density since it is significantly blended with unrelated features. For the line transitions at C I $\lambda\lambda$1560,1656 we also masked out regions of the spectrum showing unrelated absorption features, which were excluded as potential additional velocity components based on the identification in the C I λ1328 line complex. We obtain a best-fit b-parameter of $b = 2.3 \pm 0.5\,\mathrm{km\,s^{-1}}$. The line profiles seem to exclude values of $b \gtrsim 3\,\mathrm{km\,s^{-1}}$, both when considering the line widths and the relative optical depths. We therefore assume the best-fit b value throughout, but provide the derived column density for fixed $b = 5\,\mathrm{km\,s^{-1}}$ in Table B.2. The three fine-structure transitions all show roughly consistent column densities within the errors for both assumed b-parameters. For this GRB we measure a total C I column density of $\log N(\mathrm{C\,I})_{\mathrm{tot}} = 14.24 \pm 0.14$. Since the lines are not intrinsically saturated this estimate should be reliable, which is also supported by the measured C I rest-frame equivalent width following the linear relation from Fig. 7. The best fit Voigt profiles are shown overplotted on the normalized VLT/X-shooter spectrum in Fig. B.2 for $b = 2.3\,\mathrm{km\,s^{-1}}$.

Table B.2. Results of the Voigt-profile fitting for GRB 120815A.

Exc. state (J)	$\log N(\mathrm{C\,I})$ $b = 2.3 \pm 0.5$ ($\mathrm{km\,s^{-1}}$)	$b = 5$ ($\mathrm{km\,s^{-1}}$)
C I	13.94 ± 0.26	13.35 ± 0.16
C I*	13.62 ± 0.14	13.52 ± 0.11
C I**	13.66 ± 0.22	13.57 ± 0.12

B.4. GRB 120909A at z = 3.9290

The spectrum presented here was published by Selsing et al. (2019). The neutral and molecular gas-phase abundances listed in Table 1 derived for this GRB are adopted from Bolmer et al. (2019), who also reported the detection of H_2 in the spectrum. They found $\log N(\mathrm{H\,I}) = 21.82 \pm 0.02$, $\log N(\mathrm{H_2}) = 17.25 \pm 0.23$, $[\mathrm{S/H}] = -1.06 \pm 0.12$ and $[\mathrm{S/Fe}] = 0.50 \pm 0.15$, resulting in a dust-corrected metallicity of $[\mathrm{M/H}] = -0.29 \pm 0.10$. Greiner et al. (in prep.) derived a visual extinction in the line of sight to this GRB of $A_V = 0.16 \pm 0.04$ mag (see Bolmer et al. 2019). We find no evidence for C I in this absorption system (see also Heintz et al. 2019a), and derive a 2σ upper limit of $\log N(\mathrm{C\,I})_{\mathrm{tot}} < 14.0$ assuming $b = 2\,\mathrm{km\,s^{-1}}$.

B.5. GRB 121024A at z = 2.3005

The spectrum presented here was first published by Friis et al. (2015), who also reported the presence of H_2 in the spectrum. The neutral and molecular gas-phase abundances listed in Table 1 derived for this GRB are adopted from Bolmer et al. (2019). They found $\log N(\mathrm{H\,I}) = 21.78 \pm 0.02$, $\log N(\mathrm{H_2}) = 19.90 \pm 0.17$, $[\mathrm{Zn/H}] = -0.76 \pm 0.06$ and $[\mathrm{Zn/Fe}] = 0.77 \pm 0.08$, resulting in a dust-corrected metallicity of $[\mathrm{M/H} = -0.68 \pm 0.07$. We adopt the visual extinction derived by Zafar et al. (2018b) of $A_V = 0.26 \pm 0.07$ mag.

To fit the neutral atomic carbon abundances for this GRB we again ran the fit leaving b as free parameter or fixed to $b = 5\,\mathrm{km\,s^{-1}}$. We only detect a single absorption component across the four line complexes so we fixed this in the fit and masked out any unrelated or blended features. The fit was mainly constrained by the C I $\lambda\lambda$1328,1656 line transitions. The C I $\lambda\lambda$1277,1560

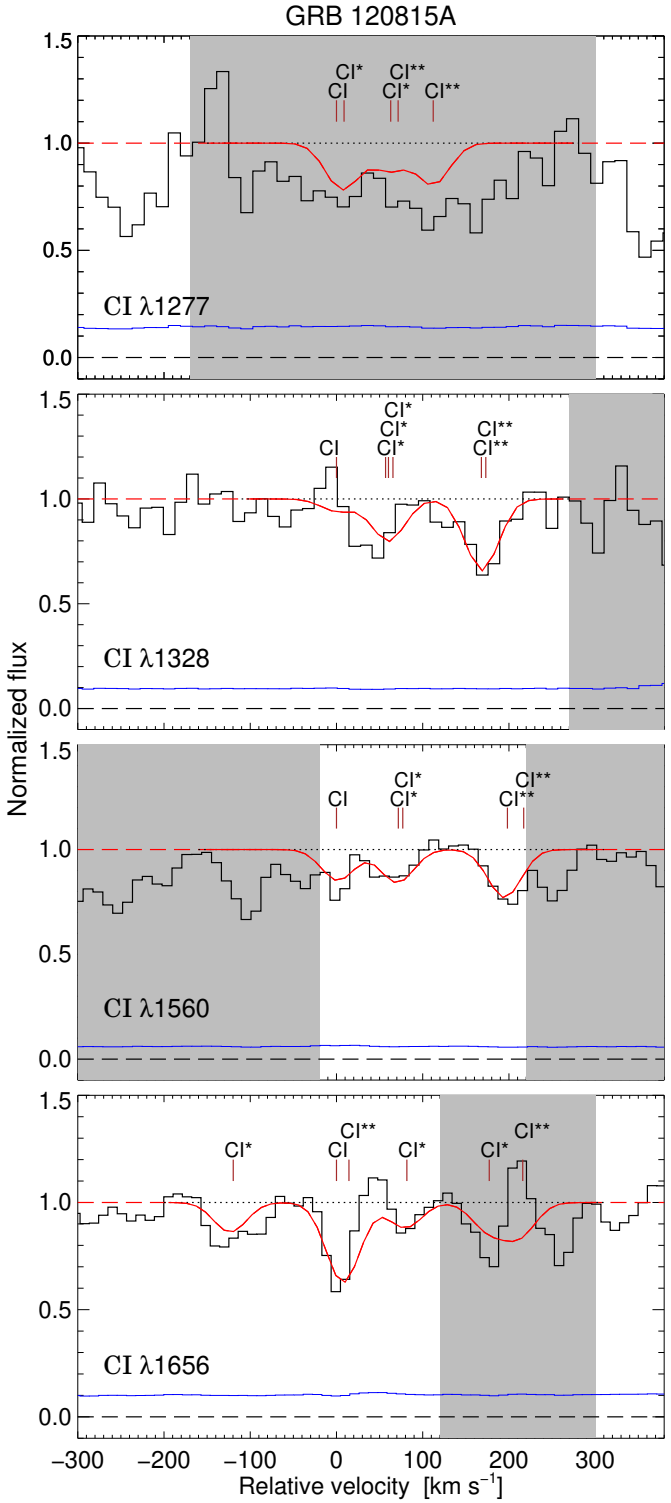

Fig. B.2. Same as Fig. B.1 but for GRB 120815A with $b = 2.3 \pm 0.5$, centered on $z = 2.35814$.

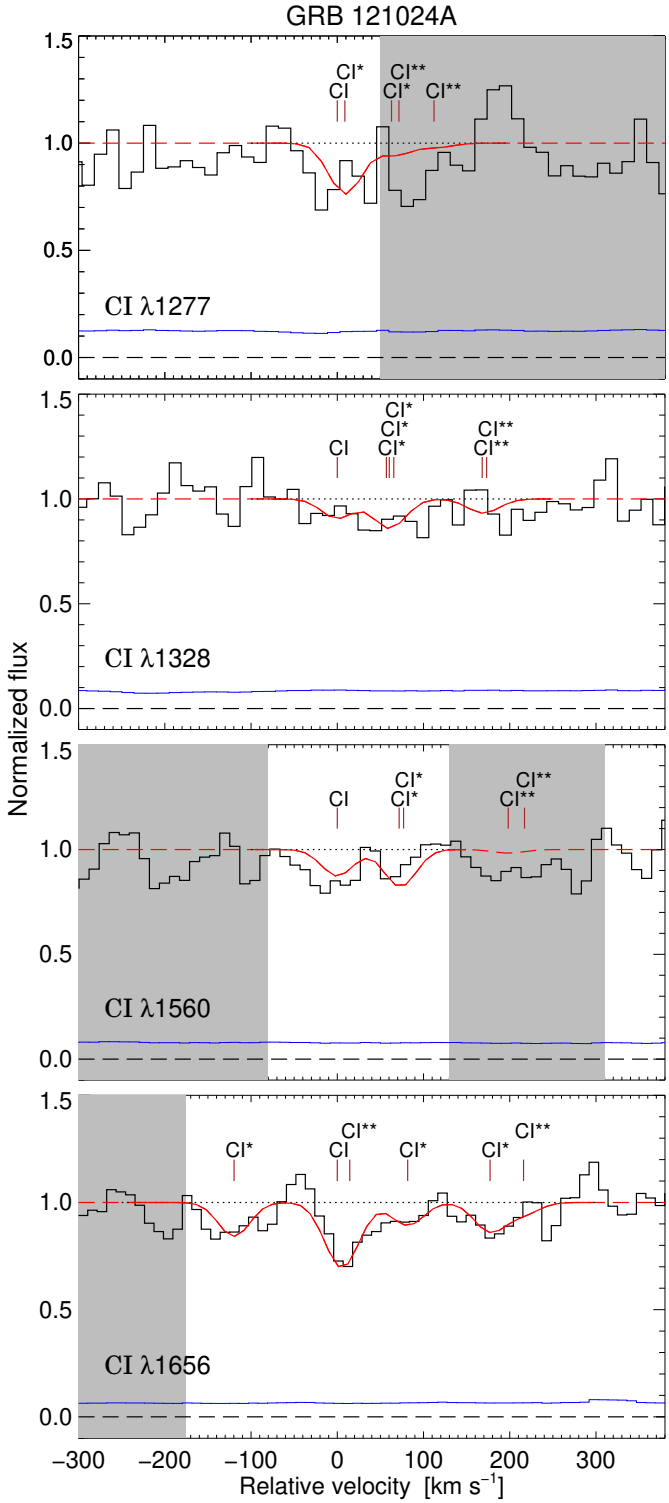

Fig. B.3. Same as Fig. B.1 but for GRB 121024A with fixed $b = 5\,\mathrm{km\,s^{-1}}$, centered on $z = 2.30208$.

lines were only used to constrain the upper limit on the column density since they are significantly blended. We obtain a best-fit b-parameter of $b = 3.5 \pm 0.5\,\mathrm{km\,s^{-1}}$. The line profiles seem to exclude values of $b \gtrsim 5\,\mathrm{km\,s^{-1}}$, both when considering the line widths and the relative optical depths. However, since we are not able to distinguish between the best-fit and fixed b-parameter of $b = 5\,\mathrm{km\,s^{-1}}$, we assume the latter column density throughout. The three fine-structure transitions also all show roughly consistent column densities within the errors for both assumed b-parameters (see Table B.3). For this GRB we measure a total C I column density of $\log N(\mathrm{C\,I})_{\mathrm{tot}} = 13.91 \pm 0.08$. Since the lines are not intrinsically saturated this estimate should be reliable, which is also supported by the measured C I rest-frame equivalent width following the linear relation from Fig. 7. The best fit Voigt profiles are shown overplotted on the normalized VLT/X-shooter spectrum in Fig. B.3 for $b = 5\,\mathrm{km\,s^{-1}}$.

B.6. GRB 141109A at z = 2.9940

The spectrum presented here was published by Selsing et al. (2019). The neutral and molecular gas-phase abundances listed in Table 1 derived for this GRB are adopted from Bolmer et al. (2019), who also reported the detection of H_2 in the spectrum. They found $\log N(\mathrm{H\,I}) = 22.18 \pm 0.02$, $\log N(H_2) = 18.02 \pm 0.12$, $[\mathrm{Zn/H}] = -1.63 \pm 0.06$ and $[\mathrm{Zn/Fe}] = 0.49 \pm 0.07$, resulting in a dust-corrected metallicity of $[\mathrm{M/H}] = -1.37 \pm 0.05$. Heintz et al. (2019a) derived a visual extinction in the line of sight to this GRB of $A_V = 0.11 \pm 0.03$ mag and also found no evidence for C I in this absorption system. We derive a 2σ upper limit of $\log N(\mathrm{C\,I})_{\mathrm{tot}} < 14.7$ assuming $b = 2\,\mathrm{km\,s^{-1}}$.

B.7. GRB 150403A at z = 2.0571

The spectrum presented here was published by Selsing et al. (2019). The neutral and molecular gas-phase abundances listed in Table 1 derived for this GRB are adopted from Bolmer et al. (2019). They found $\log N(\mathrm{H\,I}) = 21.73 \pm 0.02$, $\log N(H_2) = 19.90 \pm 0.14$, $[\mathrm{Zn/H}] = -1.04 \pm 0.04$ and $[\mathrm{Zn/Fe}] = 0.63 \pm 0.08$, resulting in a dust-corrected metallicity of $[\mathrm{M/H}] = -0.92 \pm 0.05$. We adopt the upper limit on the visual extinction derived by Heintz et al. (2019b) of $A_V < 0.13$ mag.

To fit the neutral atomic carbon abundances for this GRB we only ran iterations with fixed values of $b = 5$ and $b = 10\,\mathrm{km\,s^{-1}}$, since the fit could not converge on a realistic value for b if left as a free parameter. The fit was mainly constrained by the C I $\lambda\lambda$ 1560,1656 line transitions. The C I $\lambda\lambda$ 1277,1328 lines were masked out in the fit since they are significantly blended with tellurics. Their apparent optical depths are, however, still required to be consistent with the derived column densities. For the C I $\lambda\lambda$ 1560,1656 line transitions we also masked out regions of the spectrum showing unrelated absorption features or bad pixels with correlated noise, and therefore only fit for the same components as identified for the C I λ 1656 line complex. The observed line profiles appear to be consistent with both $b = 5$ and $b = 10\,\mathrm{km\,s^{-1}}$, so we adopt $b = 5\,\mathrm{km\,s^{-1}}$ to be consistent with the other bursts. The relative abundances for all the fine-structure transitions of the ground-state are consistent, however, within errors for both b-parameters (see Table B.4). For this GRB we derive a 2σ lower limit of $\log N(\mathrm{C\,I})_{\mathrm{tot}} \gtrsim 14.3$. This lower limit takes into account both the uncertain line broadening and the intrinsically saturated line profiles. The best fit Voigt profiles are shown overplotted on the normalized VLT/X-shooter spectrum in Fig. B.4 for $b = 5\,\mathrm{km\,s^{-1}}$.

B.8. GRB 180325A at z = 2.2496

The spectrum presented here was published by Zafar et al. (2018a), who also reported the detection of C I. The gas-phase abundances and visual extinction listed in Table 1 derived for this GRB are adopted from their work. They found $\log N(\mathrm{H\,I}) = 22.30 \pm 0.14$, $[\mathrm{Zn/H}] = > -0.96$ and $A_V = 1.58 \pm 0.12$ mag from the first epoch VLT/X-shooter observations. It was not possible to search for H_2 in this absorption system due its high visual extinction (Zafar et al. 2018a; Bolmer et al. 2019).

To fit the neutral atomic carbon abundances for this GRB we only ran iterations with fixed b-parameters, since the fit could not converge on a realistic value for b if left as a free parameter. The fit was only constrained by the C I $\lambda\lambda$ 1560,1656 line transitions since the C I $\lambda\lambda$ 1277,1328 lines were completely blended with telluric absorption features and in spectral regions with poor S/N. For the C I $\lambda\lambda$ 1560,1656 line transitions we also masked out regions of the spectrum showing unrelated absorption features. The S/N is quite poor in the spectral region around these line complexes as well, so we only perform the fit assuming a single absorption component and with b-parameters fixed to $b = 5$ and $b = 10\,\mathrm{km\,s^{-1}}$, respectively. While the observed line profiles appear to be consistent with both $b = 5$ and $b = 10\,\mathrm{km\,s^{-1}}$, the column densities derived assuming $b = 5\,\mathrm{km\,s^{-1}}$ (especially the ground-state, see Table B.5) are significantly overestimated.

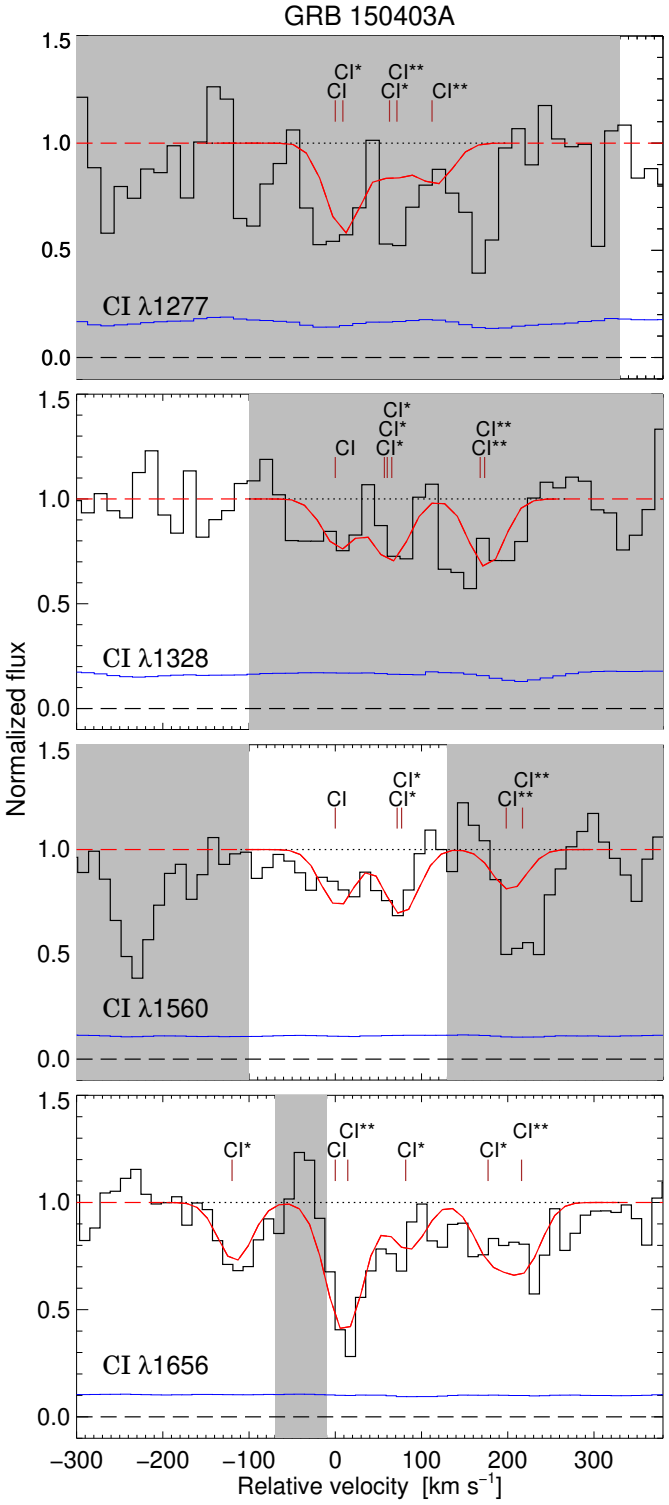

Fig. B.4. Same as Fig. B.1 but for GRB 150403A with fixed $b = 5\,\mathrm{km\,s^{-1}}$, centered on $z = 2.05691$.

Table B.3. Results of the Voigt-profile fitting for GRB 121024A.

Exc. state	$\log N$(C I) $b = 3.5 \pm 0.5$ (km s^{-1})	$b = 5$ (km s^{-1})
C I	13.61 ± 0.17	13.40 ± 0.15
C I*	13.81 ± 0.10	13.60 ± 0.09
C I**	13.70 ± 0.17	13.23 ± 0.21

Table B.4. Results of the Voigt-profile fitting for GRB 150403A.

Exc. state	$\log N$(C I) $b = 5$ (km s^{-1})	$b = 10$ (km s^{-1})
C I	14.12 ± 0.29	13.74 ± 0.13
C I*	14.15 ± 0.15	13.90 ± 0.07
C I**	14.50 ± 0.39	14.08 ± 0.12

Table B.5. Results of the Voigt-profile fitting for GRB 180325A.

Exc. state	$\log N$(C I) $b = 5$ (km s^{-1})	$b = 10$ (km s^{-1})
C I	17.32 ± 0.17	14.50 ± 0.31
C I*	14.98 ± 0.27	14.25 ± 0.11
C I**	14.51 ± 0.30	14.20 ± 0.20

We therefore adopt $b = 10\,\mathrm{km\,s^{-1}}$ and derive a 2σ lower limit of $\log N(\mathrm{C\,I})_{\mathrm{tot}} \gtrsim 14.5$ for this GRB. This lower limit takes into account both the uncertain line broadening and the intrinsically saturated line profiles. The best fit Voigt profiles are shown overplotted on the normalized VLT/X-shooter spectrum in Fig. B.5.

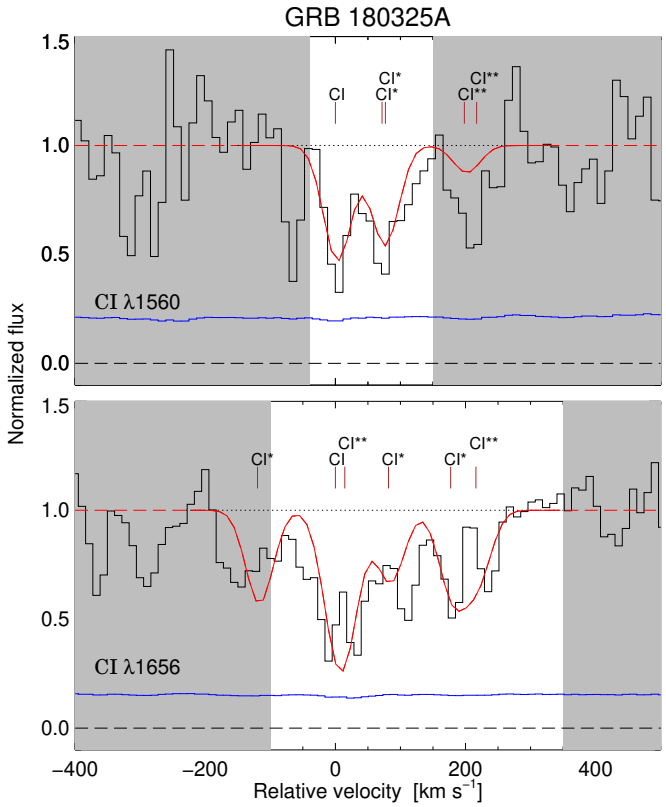

Fig. B.5. Same as Fig. B.1 but for GRB 180325A with fixed $b = 10\,\mathrm{km\,s^{-1}}$, centered on $z = 2.24954$.